Production Engineering
https://doi.org/10.1007/s11740-025-01374-7

ORIGINAL PAPER

Experimental and multiscale simulation analysis of the lubricant penetration in gear skiving

Edder J. García[1,2] · Florian Sauer[3] · Matthias Haber[4] · Amartya Mukherjee[3] · Kerstin Falk[2] · Corina Schwitzke[4] · Hans-Jörg Bauer[4] · Michael Moseler[1,2] · Volker Schulze[3]

Received: 30 June 2025 / Accepted: 29 August 2025

Abstract
Cooling lubricants play essential roles in machining processes, namely cooling and lubricating contact surfaces, and facilitating the removal of chips that could compromise surface quality. A key question is how well the lubricant penetrates the cutting zone in complex interrupted cutting operations, such as gear skiving. This study tackles the challenge of analyzing the behavior of cooling lubricants across different scales by employing a combined experimental and multiscale simulation approach. The overall fluid flow is modeled using smoothed particle hydrodynamics, while chip formation is simulated with finite element methods. The cavitation behavior of the lubricant within the cutting wedge is examined using the Reynolds equation, and the tool's indentation is investigated through molecular dynamics simulations. Finite element simulations are validated against experimental data from gear skiving tests using AISI 4140 steel, showing an average deviation of 6.6% in the maximum force values. Smoothed particle hydrodynamics simulations predict that the cooling lubricant can reach the meshing zone between the tool and the workpiece. For validation purposes, typical global flow characteristics from the simulation are compared with high-speed camera images, exhibiting good agreement. In typical gear skiving conditions, Reynolds calculations indicate that significant cavitation occurs, resulting in a substantial portion of the contact area remaining dry. We investigate the conditions that can help reduce cavitation. Molecular dynamics simulations reveal that nanocavities on the tool's surface can improve the transport of lubricant molecules to the contact area.

Keywords Multiscale modeling · Gear skiving · Reynolds · Molecular dynamics · Cavitation · Smoothed particle hydrodynamics

1 Introduction

The field of machining is highly dependent on the effects of cooling lubricants, which perform a variety of functions, including enhancing heat dissipation [1], reducing tool wear by decreasing friction [2], and improving surface finishing to ensure efficient and precise machining outcomes [3]. The performance of cutting fluids is influenced by the state of the cutting conditions [4], but the conventional objective of these fluids remains unchanged: to prevent the tool and the

Edder J. García, Florian Sauer, Matthias Haber and Amartya Mukherjee contributed equally to this work.

✉ Edder J. García
edder.garcia@fmf.uni-freiburg.de

Florian Sauer
florian.sauer@kit.edu

Matthias Haber
matthias.haber@kit.edu

Amartya Mukherjee
amartya.mukherjee@kit.edu

[1] FMF Freiburg Materials Research Center, University of Freiburg, Stefan-Meier-Straße 21, 79104 Freiburg, Germany

[2] Fraunhofer IWM, MikroTribologie Centrum µTC, Wöhlerstraße 11, 79108 Freiburg, Germany

[3] WBK Institute of Production Science, Karlsruhe Institute of Technology, Kaiserstraße 12, 76131 Karlsruhe, Germany

[4] ITS Institute of Thermal Turbomachinery, Karlsruhe Institute of Technology, Straße am Forum 6, 76131 Karlsruhe, Germany

Published online: 30 October 2025

workpiece from reaching extreme temperatures [5]. Despite their widespread use, the behavior of cooling lubricants in complex machining operations remains poorly understood. While lubricants can significantly reduce friction and extend tool life in high-precision applications [6], their effectiveness varies considerably with coolant pressure[7], delivery method, and application strategy [8]. Additionally, there are conflicting research findings about the comparative benefits of wet and dry machining under various cutting conditions. These discrepancies impact crucial factors such as surface integrity [9], tool wear [10, 11], and tool lifespan [12]. This highlights the need for a more fundamental understanding of coolant behavior at multiple length scales.

Gear skiving has emerged as a critical manufacturing process for producing high-precision internal gears, particularly in the automotive industry, where lightweight and efficient transmission systems are increasingly demanded. Therefore, optimizing gear skiving is highly desirable. The aim is to improve process precision, tool life, and surface quality. Unlike conventional gear cutting processes, skiving involves complex three-dimensional kinematics with interrupted cutting that presents unique challenges for coolant delivery and effectiveness [13]. Intriguingly, recent research has revealed counterintuitive findings regarding coolant application in gear skiving. Stadtfeld [13] argues that the absence of cooling lubricants and the increase in heat generation can actually improve plastic deformation and extend the tool life of coated carbide tools. This effect is due in part to a 15% reduction in power consumption during dry skiving. The central idea of the study was to transfer as much heat as possible to the chips. As the chip shears away from the contact zone, heat is dissipated, thus cooling the contact zone. In addition, a systematic study by Arndt et al. [14] on coated carbide tools in dry and wet gear skiving revealed that dry cutting conditions are preferable to improve tool longevity. However, it also revealed that under dry conditions, the surface quality of the workpiece deteriorates significantly when using worn tools. This complex interplay of lubricants and gear skiving performance highlights the need for a more comprehensive understanding of the multi-scale effects of cooling lubrication on the skiving process. In practice, fluid interactions at nano and macro scales are interconnected, with each regime contributing distinct mechanisms that influence the solid surface wetting [15]. Therefore, the penetration of the cooling lubricant in the contact zone between the tool and the chip is the key and remains a topic of debate. Early work by Williams and Tabor [16] suggested that fluids are largely absent in the contact zone due to the very low relative sliding speed and the presence of high localized pressures between the chip and the tool. More recently, Sauer et al. [17] stated that when cutting fluid is applied at a pressure of 0.6 MPa, up to 32% of the tool-chip contact zone remains dry under most combinations of cutting parameters. It was also revealed that there is a correlation between the dry zone and the length of the sticking zone of the contact. It should be noted that the study was conducted under the limitation of 2D cutting simulations.

The complex nature of coolant behavior in machining necessitates modeling approaches that span multiple length and time scales. Traditional finite element methods (FEM), while effective for macroscopic cutting mechanics, cannot capture the fundamental molecular-level interactions that govern lubricant behavior at interfaces. This limitation has driven the development of multiscale simulation frameworks that combine different numerical techniques to address specific physical phenomena across relevant scales. At the continuum scale, smoothed particle hydrodynamics (SPH) has emerged as a powerful tool for modeling large-scale fluid flow with complex geometries and free surfaces. Its meshless nature makes it particularly suitable for simulating the dynamic fluid-solid interactions inherent in machining processes [18, 19]. For intermediate scales, the Reynolds equation with cavitation modeling provides insights into lubricant film behavior under high-pressure conditions, capturing the transition between full-film and boundary lubrication regimes [20]. At the molecular scale, molecular dynamics (MD) simulations offer unprecedented insight into interfacial phenomena that control wetting, adhesion, and transport properties. Since the pioneering work of Alder and Wainwright [21] and early applications to cutting by Belak and Stowers [22, 23], MD has evolved into a sophisticated tool for understanding nanoscale tribological phenomena. Modern multiscale approaches effectively combine MD with continuum methods. For example, Sun et al. [24] demonstrated the prediction of surface characteristics including roughness and residual stress using a MD-FEM technique, while Holey et al. [25] developed physics-based friction models for FEM simulations through density functional theory-based MD calculations. Despite these advances, a comprehensive multiscale framework specifically addressing coolant penetration and distribution in three-dimensional gear skiving operations remains absent from the literature. The complex interplay between global fluid delivery, local penetration mechanisms, and molecular-scale interfacial phenomena requires an integrated approach that has not been previously attempted.

This paper addresses the critical knowledge gap in understanding coolant behavior during gear skiving through a comprehensive multiscale simulation framework. Our investigation is guided by the following research questions:

1. **Effect of the lubricant on cutting forces**: Does the lubricant have an effect on the cutting forces?

2. **Global lubricant delivery**: Can the cooling lubricant effectively reach the meshing zone between the tool and the workpiece during three-dimensional gear skiving operations?
3. **Local penetration mechanisms**: What factors control the penetration of the lubricant into the cutting wedge, and under what conditions does cavitation occur?
4. **Molecular-scale transport**: How does the tool's surface topography affect the transport of lubricant molecules into the direct tool-chip contact regions?
5. **Process optimization**: How do chip velocity, coolant pressure, and chip tool opening angle influence the extent of dry contact zones, and what optimal parameter combinations can achieve maximum lubricant penetration in the tool-chip interface?

To address these questions, we employ an integrated multiscale approach combining: (i) experimental cutting tests under typical gear skiving conditions, (ii) SPH simulations for global fluid flow analysis to determine coolant accessibility to the cutting zone; (iii) FEM simulations for chip formation mechanics with experimental validation; (iv) Reynolds equation modeling with cavitation to quantify lubricant penetration and film thickness distribution; and (v) classical MD simulations to investigate molecular-scale transport mechanisms and the role of tool surface nanoroughness in the cutting process. Figure 1 gives a schematic representation of the methods used in this work.

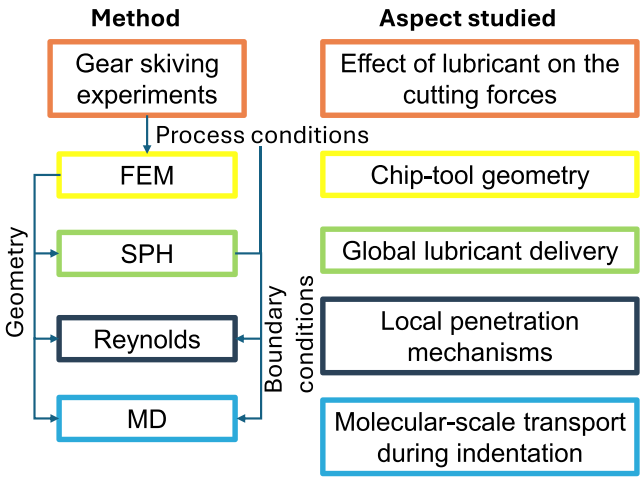

Fig. 1 Schematic representation of the different methods in the global modeling approach and the aspects studied for each method

This comprehensive methodology provides unprecedented insight into coolant behavior across all relevant length scales, from global flow patterns to molecular-level interfacial phenomena. The findings are expected to inform process optimization strategies that enhance tool life and surface quality while potentially reducing coolant consumption through improved delivery efficiency. Gear skiving experiments on AISI 4140 steel (42CrMo4) ensure practical relevance and validate the predictions of the FEM simulation.

2 Experimental methods

The experimental cutting tests were carried out using samples of AISI4140 with initial dimensions of $\varnothing 180 \times 30\,\mathrm{mm}$, which were previously quenched and tempered at 600 ° C for one hour according to DIN EN ISO 18265. The resulting hardness is $339 \pm 10\,\mathrm{HV30}$, which gives a tensile strength of $1070 \pm 31\,\mathrm{MPa}$ according to DIN EN ISO 18265. The chemical composition of the material is given in Table 1. The typical microstructure of the AISI 4140 workpiece material was examined using a Keyence VHX-7000 digital microscope, and a representative image has been included in Appendix A. This characterization provides additional insight into the material condition following heat treatment.

The investigated gear skiving process enables efficient production of internal gears used in electric vehicle transmission system. Taking these scenarios into consideration, the properties of the workpiece and tool, in addition to the process-related conditions, are shown in Table 2.

The gear skiving experiments were carried out on a PV315 SkivLine from Pittler T & S GmbH. The test setup, as shown in Fig. 2, consists of the tool, which is mounted on a Kistler 9124B rotating force measuring platform, and the clamping of the workpiece with a three-jaw pendulum chuck. An simplified tool setup with a single-tooth cutting insert was used for the tests, enabling in-depth observation of the cutting behavior during single-tooth engagement. The tool inserts are made of K30 carbide and coated with AlCrN using the Alcrona Pro process by Oerlikon Balzers. The force values are divided into the axial feed direction along the z-axis and the cutting force components along the x and y axes. The forces are recorded as a rotating coordinate system. Then a time-synchronized mean value is calculated from the measured force data. To compare the forces with the FEM simulation results, the recorded measurement

Table 1 Chemical composition of AISI4140 steel (wt%)

C	Mn	Si	P	S	Cr	Mo	Cu
0.41	0.81	0.33	0.01	0.023	1.04	0.189	0.13

Table 2 Workpiece, tool and process data of the gear skiving process

Workpiece data					
Number of teeth	z_2	-96	Helix angle	β_2	22.54°
Tip diameter	d_{a2}	135.8 mm	Root diameter	d_{f2}	143.2 mm
Normal pressure angle	α_n	17.5°	Normal module	m_n	1.34 mm
Profile shift	x_E	0.138	Tooth width	b_2	27.2 mm
Tool and process data					
Number of teeth	z	48(1)	Helix angle	β_0	-0.03°
Tip diameter	d_{a0}	68.68 mm	Root diameter	d_{f0}	60.4 mm
Constructive head clearance angle	α_c	0°	Stair angle	τ	0°
Position Angle	κ_2	25.9°	Axis crossing angle	Σ	24.75°
Normal module	m_n	1.34 mm	Profile shift	x	-0.002

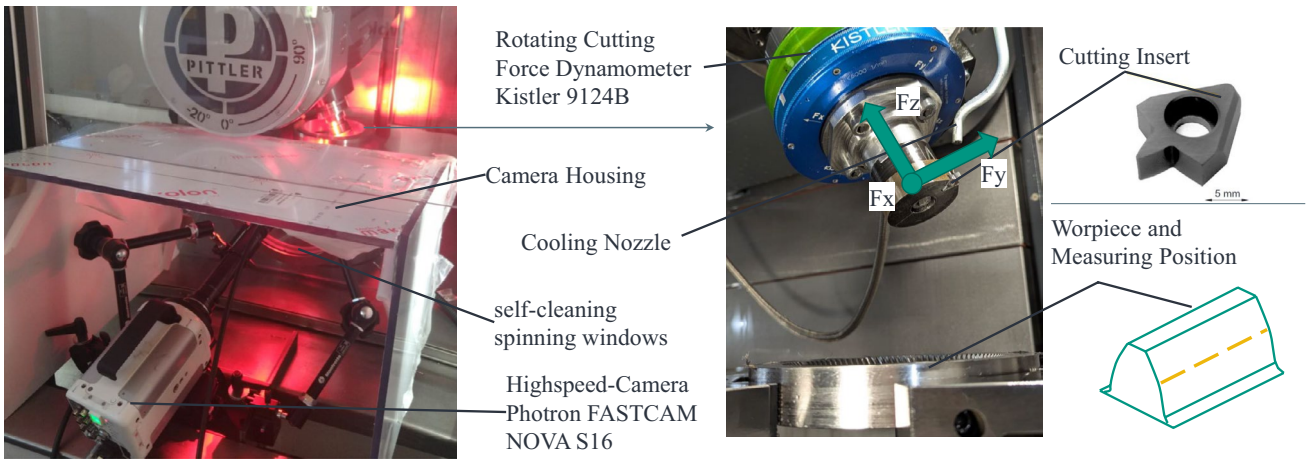

Fig. 2 Experimental setup of gear skiving process on a PV315 SkivLine

are then transformed into a stationary machine coordinate system using coordinate transformation. The supply of compressed air and oil to the cutting point is stationary in the area of the pressure angle κ_2, parallel to the workpiece axis.

A special setup was developed to investigate the global flow characteristics of the gear skiving process under the presence of oil. This consists of an enclosure for the Photron FASTCAM NOVA S16 high-speed camera and a Rotoclear S3 self-cleaning window positioned in front of the camera lens. The window ensures that the recorded videos are not affected by oil spray. A Navitar 12x zoom lens with a 0.25 attachment lens was used for the recordings. The recordings were made at a frame rate of 16,000 frames per second. In order to investigate the influence of the cooling lubricant on the formation of the chips, the chips were collected during the tests and subsequently geometrically measured using a Zeiss CT Metrotom 800 computer tomograph. The open-source software Cloudcompare [26] was utilized to evaluate the geometric disparities between the chips with and without cooling lubricant. After completion of the tests, the surface roughness of the leading and trailing flanks was measured. For this purpose, five teeth were removed from the workpiece and the corresponding flank lines were measured at the level of the pitch circumference using a MarSurf XCR 20.

3 Numerical modeling

3.1 FEM simulations

Simulations of chip formation during gear skiving were performed using Simufact Forming 2024 with the MARC solver. The simulations were performed using implicit time integration with the dynamic transient operator Single-Step Houbolt for dynamic time-step analysis. A multifrontal direct sparse solver with a complete Newton-Raphson iteration method was selected. The time step size was selected based on the minimum element edge length and the cutting speed to ensure a stable simulation of the cutting process. The model consists of a rigid tool with a variable tri-mesh and heat sinks that specify the thermal boundary conditions of the workpiece and the tool. To optimize the calculation time, the ideal tooth flank contour, as shown in Fig. 3a for the last depth of cut, was exported using OpenSkiving [27]. The exported tooth flank adequately represents the transition from the depth of cut nine to the last infeed. In Fig. 3a, this is indicated by the contact line of the tool. In the next step, the exported three-dimensional surface mesh is converted into a volume body required for the simulation of chip formation (see Fig. 3b). In addition, the workpiece is

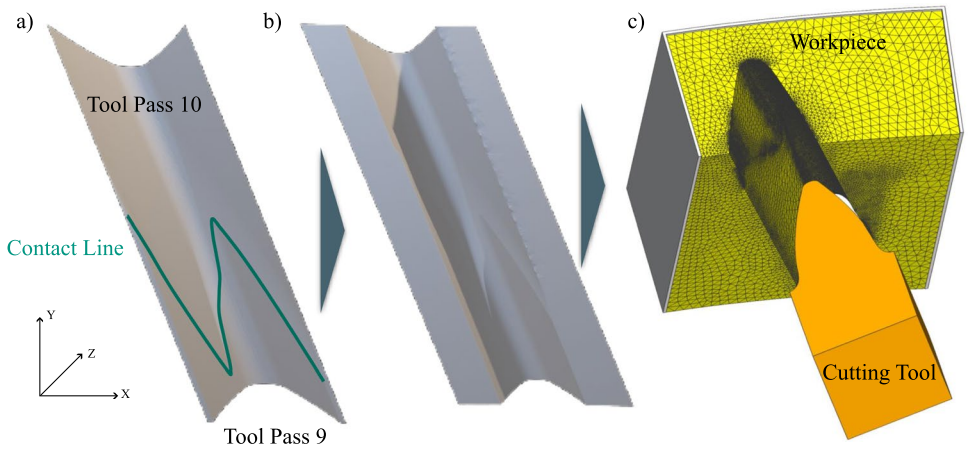

Fig. 3 Simulation setup for gear skiving during the final infeed stage

Table 3 Fitted pressure dependent friction parameters [25]

a	b	τ_0
(-)	(-)	(GPa)
0.038	0.031	2.240

Table 4 Johnson-Cook parameters for material modeling in FEM simulations

A	B	C	n	m
(MPa)	(MPa)	(-)	(-)	(-)
595	580	0.023	1.03	0.133

constructed with a triangular element mesh, with continuous remeshing triggered by excessive element distortion, strain change, and tool penetration, resulting in a minimum element edge length of 10 µm, as shown in Fig. 3c.

For the contact formulation, a node segment approach is used, in which the contact of deformable bodies with a rigid body is handled using a single-point constraint equation (SPC). The stick-sliding friction model developed by Holey et al. [25], which was previously investigated for orthogonal cuts within the gear skiving framework [28], was used:

$$\tau_{\mathrm{f}}(\sigma_{\mathrm{n}}) = \begin{cases} \mu(\sigma_{\mathrm{n}})\sigma_{\mathrm{n}}, & \sigma_{\mathrm{n}} < p_{\mathrm{Y}}, \\ k(\sigma_{\mathrm{n}}), & \sigma_{\mathrm{n}} \geq p_{\mathrm{Y}}, \end{cases} \tag{1}$$

with $\mu(\sigma_{\mathrm{n}}) = k(\sigma_{\mathrm{n}})/p_{\mathrm{Y}}$ and $k(\sigma_{\mathrm{n}}) = \tau_0 + a\sigma_{\mathrm{n}} + b\sigma_{\mathrm{n}}^2$ and the parameters are shown in Table 3.

The Johnson-Cook plasticity model [29] is used to model the workpiece material, as it is a widely applied model in machining simulations.

$$\sigma_{\mathrm{f}} = [A + B\bar{\epsilon}^n]\left[1 + C\ln\left(\frac{\dot{\epsilon}}{\dot{\epsilon}_0}\right)\right]\left[1 - \left(\frac{T - T_{\mathrm{room}}}{T_{\mathrm{m}} - T_{\mathrm{room}}}\right)^m\right], \tag{2}$$

where σ_{f} represents the temperature and strain rate dependent plastic flow stress. The model parameters are given in Table 4 according to previous work [17, 25], where A is the yield strength, B is the hardening modulus, C is the strain rate sensitivity coefficient, n is the hardening coefficient, and m is the thermal softening coefficient.

Table 5 Constant parameters used in the FE simulations

T_{m}	T_{room}	λ_c	$\dot{\epsilon}_0$	α_{air}	α_{oil}
K	K	W/mK	(-)	W/m^{2}K	W/m^{2}K
1820	298	120	1	23	2500

Furthermore, the temperature-dependent properties of the investigated material AISI4140 were taken from the [30–32].

Based on the actual geometry of the tool that was measured optically with a Keyence VHX-7000, the cutting-edge rounding was set to 20 µm.

The parameters that were constant during the simulation are listed in Table 5. The heat transfer coefficients to the environment were varied according to the cooling method as described in Ref. [33].

In this study, we introduce the term "chip opening angle" ($\gamma_{opening}$) to describe the angle formed by the chip and the tool immediately after the chip separates from the tool. Specifically, it is the angle between vectors **A'B'** (along the rake face) and **A'C'** (along the chip surface), where point A' is the chip detachment point, and points B' and C' can be defined at a distance L away from A' on the rake face and chip surface, respectively. The opening angle is illustrated schematically in Fig. 6. This metric quantifies the chip's initial divergence from the tool surface and provides insight into how the chip behaves under different cutting conditions. The chip opening angle depends heavily on the position L at which it is measured. As the chip curls, the angle between the rake face and the chip surface increases. To ensure consistency and relevance with the actual interaction zone between the chip and the tool, the chip opening angle was measured at 100 µm from the separation point. At this distance, the chip-tool geometry can be approximated by a wedge, which is a suitable simplified geometry for hydrodynamic modeling. Moreover, this distance corresponds to the area of high normal and shear stress, where

lubrication behavior is most critical and can be effectively approximated by the Reynolds model. The resulting opening angles, sampled across various FEM simulation cases examined in a previous study [28], are shown in Fig. 4. For each test case, the standard deviation represents the variation in the chip opening angle at different time steps.

3.2 SPH simulations of the global fluid distribution

In this section, the methodology for simulating the global fluid distribution is briefly explained. The purpose of these simulations is to predict the fluid distribution, particularly in the proximity of the meshing zone between the tool and workpiece where the chip is formed. The results indicating whether the tool and workpiece are wetted when cutting begins provide important information about the initial conditions for the smaller-scale investigations (Reynolds calculations and molecular dynamics) presented later.

3.2.1 Methodology

Given the intricate geometric configuration—particularly the complex kinematics and the presence of multiphase flow phenomena, along with pronounced fluid deformation and rotational velocities—the application of a mesh-free Lagrangian numerical approach offers notable advantages over conventional grid-based computational fluid dynamics (CFD) techniques, as demonstrated by Keller et al. [34] and applied on epicyclic gear trains by Haber et al. [35]. Since the influence of multiphase effects is considered negligible in this context, the present study adopts a single-phase modeling strategy incorporating a free-surface representation. This methodological choice is primarily motivated by considerations of computational efficiency, as fully resolved multiphase simulations entail substantial numerical cost. Smoothed Particle Hydrodynamics (SPH) is a mesh-free, Lagrangian numerical method initially developed within the field of astrophysics by Lucy [36] and Monaghan [37].

In SPH, the fluid domain is discretized into a finite set of moving interpolation points, commonly referred to as particles. Each particle represents the local physical properties of the fluid. The fundamental idea of the method lies in the discretization of spatial field variables and their differential operators, which is achieved through the use of the Dirac-δ identity. This identity asserts that the convolution of a continuous, compactly supported function $f(\vec{r})$ with the Dirac-δ distribution yields the function itself:

$$f(\vec{r}) = \int f(\vec{r'})\delta(\vec{r} - \vec{r'})d\vec{r'}. \tag{3}$$

By replacing the Dirac-δ in Eq. 3 with a smoothing function $W(\vec{r} - \vec{r'}, h)$, known as a kernel, and also replacing the analytic integral with a sum over the neighboring particles j of a center particle i, the SPH approximation can be formulated as

$$f(\vec{r}_i) \approx \sum_j f(\vec{r}_j)W(\vec{r}_i - \vec{r}_j, h). \tag{4}$$

The variable h denotes the smoothing length of the kernel, which is related to radius of influence. This approach is used to discretize the governing equations, which are given in Lagrangian form. These are essentially the mass balance equations

$$\frac{D\rho}{Dt} = -\rho(\vec{\nabla} \cdot \vec{v}), \tag{5}$$

which describes the change in density ρ of a fluid element resulting from spatial variation in its velocity $\vec{v}$, and the equation of balance of momentum.

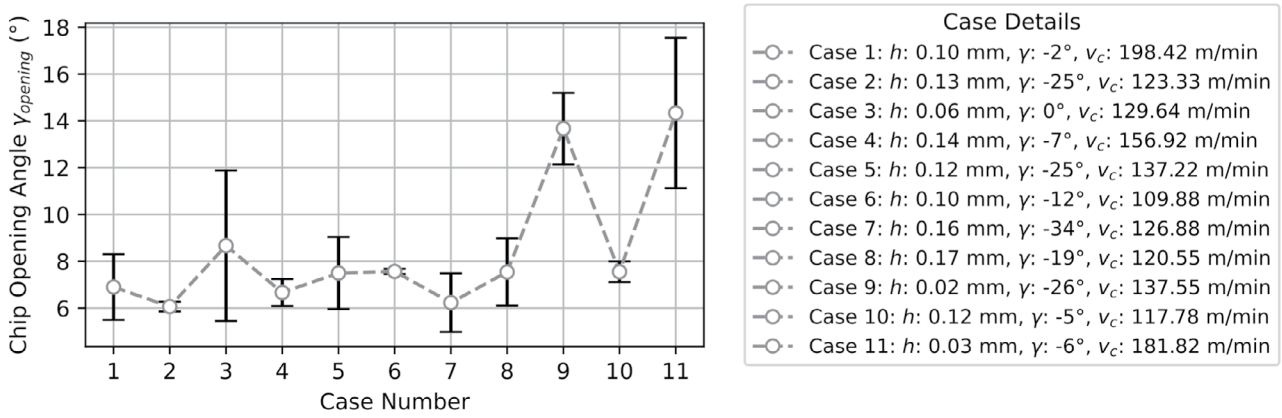

Fig. 4 Chip opening angles for various cutting conditions, measured at 100 μm from the chip detachment point. Error bars indicate standard deviation over multiple time steps for each specific test case

$$\frac{D\vec{v}}{Dt} = -\frac{\vec{\nabla}p}{\rho} + \frac{1}{\rho}\vec{\nabla}\cdot\boldsymbol{\tau} + \vec{f}_\sigma + \vec{f}_b. \tag{6}$$

This equation describes the acceleration of an element of fluid due to normal stresses from static pressure p, viscous shear stresses represented by the tensor $\boldsymbol{\tau}$, surface tension forces $\vec{f}_\sigma$, and body forces $\vec{f}_b$ like gravitation. More detailed information on the modeling approaches for each term is presented in Aguirre Bermudez et al. [38].

To effectively resolve complex geometrical features, substantial fluid deformation, and rotational dynamics, the Implicit Incompressible Smoothed Particle Hydrodynamics (I-ISPH) method is employed in the formulation, which is suggested by Ihmsen et al. [39]. Simulations are carried out within the commercial SPH solver PreonLab®. Surface tension is modeled in a manner similar to that described by Akinci et al. [40].

3.2.2 Simulation setup

As depicted in Fig. 2, the key components in this single-tooth gear skiving setup are the tool with the cutting insert and the workpiece. These simplified geometries are shown in Fig. 5. The workpiece is essentially an annular body that is clamped into the machine. To facilitate the execution of single-tooth gear skiving experiments, the inner protruding section of the ring, which is subject to machining, is reinserted into the ring for each test run.

As chip formation is beyond the scope of this simulation of global fluid distribution, a major simplification is introduced: The chip itself is not considered. Consequently, the tooth gap is modeled as the final machined geometry after the last infeed. Thus, the cutting insert never intersects the workpiece, but only contacts the tooth flanks.

The prescribed kinematics of the bodies are inherited from the gear skiving process as described in Section 2. According to Table 6 the workpiece rotates around the machine z-axis with the rotational speed ω_w. However, the tool rotates around its own center axis with the rotational speed ω_t and is simultaneously translated with the velocity $v_{\mathrm{t,z}}$ parallel to the machine z-axis.

As depicted in Fig. 5 three different nozzle positions (A, B, C) for injecting the cooling oil into the gear skiving setup are investigated. The nozzle remains stationary in the machine's reference system. Generally, the nozzle center axis is always aligned parallel with the z-axis. In configuration B, the nozzle axis is directed precisely toward the meshing region between the tool tip and the workpiece tooth gap. Compared to Position B, the nozzle is $\pm 20°$ rotated around the machine z-axis to reach configurations C and A, respectively. At a distance of 30 mm above the top surface of the workpiece, the oil particles are injected with an circular inlet boundary condition. Its diameter is set to 4 mm, in accordance with the experimental setup. A volumetric flow rate of 7.0 $\mathrm{dm^3\ min^{-1}}$ is prescribed with a parabolic shaped velocity profile. The physical properties of the Fuchs Ecocut 715 LE oil used in this study are presented in Table 7.

Surface tension, as well as the advancing and receding dynamic-contact angles, were measured with a tensiometer from the company KRÜSS, applying the Wilhelmy Plate method [41]. These measurements were performed for the pairing of AISI4140 material with Ecocut 715 LE oil. The oil is discretized with a particle resolution of 100 µm. A

Table 6 Kinematic Boundary Conditions

Workpiece	Tool	
ω_w $(\mathrm{min^{-1}})$	ω_t $(\mathrm{min^{-1}})$	$v_{\mathrm{t,Z}}$ (m/min)
715.785	1431.000	-0.301

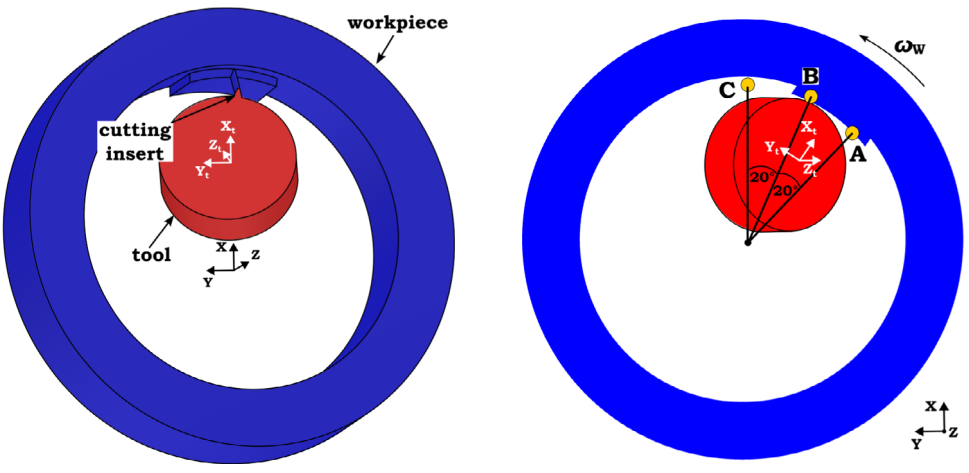

Fig. 5 (a) Simplified gear skiving geometry and (b) Nozzle positions from top for the configurations A to C

Table 7 Physical Properties of Fuchs Ecocut 715 LE at 20°C

Density	Kin. Viscosity	Surface Tension	Adv. Contact Angle	Rec. Contact Angle
(kg/m^3)	(mm/s^2)	(mN/m)	(○)	(○)
890	42	29.0	35.2	27.2

cylindrical shaped outlet boundary condition that encloses the entire setup is placed at sufficient distance (min. 15 cm) from the rigid bodies in order to remove oil particles once they leave the domain of interest. This helps to limit the particle count during the simulation in an order of 5×10^6.

Fluid–solid interaction is modeled using a particle–particle approach. The surfaces of the rigid bodies are discretized with wall particles. During the simulation, fluid particle pressure is transferred to nearby solid particles. The particle velocities are adjusted using the non-slip boundary condition by Hu and Adams [42], which introduces virtual particles mirrored inside the solid when the fluid particles overlap the wall boundary. These virtual particles replicate the properties of the fluid.

3.3 Reynolds calculations

The lubricant penetration into the cutting wedge was modeled using the steady one-dimensional Reynolds equation, incorporating cavitation via a mass conserving approach that satisfies the Jakobsson–Floberg–Olsson (JFO) conditions, given by

$$\frac{\partial}{\partial x}\left(\frac{\rho}{12\eta}h^3\frac{\partial p}{\partial x}\right) = \frac{v}{2}\frac{\partial[(1-\theta)\rho h]}{\partial x} \tag{7}$$

where x is the spatial dimension, η is the dynamic viscosity, ρ is the density, $h(x)$ is the film thickness, $p(x)$ is the pressure, $v(x)$ is the chip sliding velocity, and $\theta(x)$ is the cavitation fraction (where $\theta(x) \in [0, 1]$, with $\theta = 0$ for a full film).

The Reynolds equation was solved using complementary constraints: $p\ \theta > 0,\ p \geq 0,\ \theta \geq 0$. The lubricant's density is treated as constant. This approach is justified because the variation in density within the considered pressure range (0 - 100 MPa) is less than 2%. The fluid is modeled as piezo-viscous, applying the Barus equation. The parameters for the Barus equation were determined using non-equilibrium MD simulations. More details are provided in Appendix B. The cavitation pressure was zero ($p_{cav} = 0$).

The sketch of the system being analyzed with the Reynolds calculations domain is shown in Fig. 6. The boundary conditions were established as follows. On the right side, the entrance of the wedge is directly connected to the lubricant reservoir, which is maintained at the feeding pressure p_f. Thus, Dirichlet boundary conditions were applied on the right boundary, where $p_f = 0.6$ MPa and $\theta = 0$. The feeding pressure was taken from computational fluid dynamics from our previous work [17]. On the left side, the contact is closed ($h_{min} = 0$), resulting in zero mass flow. Neumann boundary conditions, $\frac{dp}{dx} = 0$, can be applied on the left side for pressure. However, in the case where $h_{min} = 0$ naturally imposes a zero mass flow condition, making the need for a boundary condition for the pressure on the left side irrelevant. This type of natural boundary condition is commonly observed in mixed lubrication regimes, where fully lubricated zones are in contact with areas experiencing dry solid-to-solid contact [43].

The Reynolds equation was solved using the Fischer-Burmeister-Newton-Schur (FBNS) algorithm [20, 44]. A total of 800 nodes were utilized, for a domain length of $L = 100\ \mu$m, thus $\Delta x = 0.125\ \mu$m. The velocity of the chip was systematically varied between 0.1 and 3.0 m/s, which are typical velocities in gear skiving [17]. The penetration of the lubricant was quantitatively analyzed by identifying the position of the contact line between the liquid phase ($\theta = 0$) and the vapor phase ($\theta = 1$). The contact line was defined as the location along the x axis where the

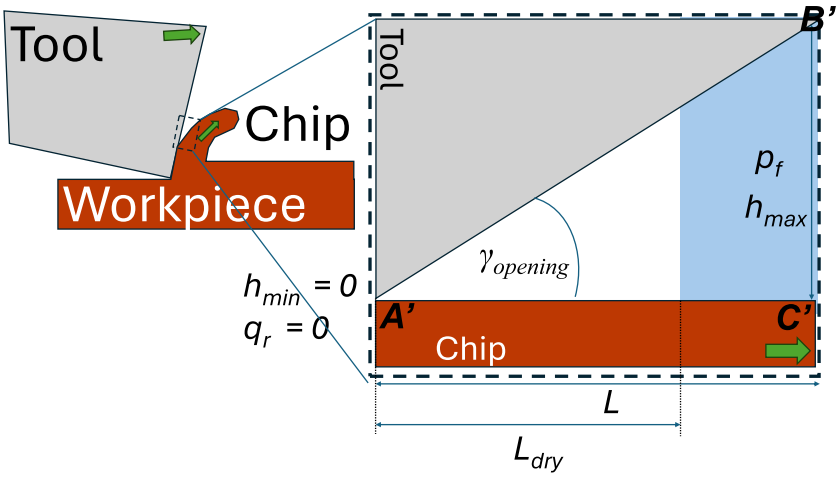

Fig. 6 Schematic representation of the geometry, boundary conditions, and illustration of the parameters for Reynolds calculations. The parameters h_{min} and h_{max} are the minimum and the maximum of the cutting wedge, p_f is the pressure at which the lubricant is applied, and q_r is the mass flow rate. The shaded blue area represents the liquid phase ($\theta = 0$), and the white area represents the cavitation zone ($\theta = 1$).

derivative of the cavitation fraction reaches its maximum, i.e. $\max_{x\in[0,L]}\left(\frac{\partial\theta(x)}{\partial x}\right)$.

3.4 MD simulations

MD simulations were performed to investigate the initial stage of the cutting process, i.e., the indentation step. MD studies on the machining of surfaces with fully submerged tools in lubricants are limited [45, 46]. These studies have shown that during the indentation step, the lubricant is completely squeezed out, leaving the contact between the tool and the workpiece dry. Notably, all of these studies have focused on atomically flat crystalline surfaces. Our objective is to determine whether nanocavities on the tool surface can prevent the complete squeeze-out of lubricant from the contact area.

3.4.1 Simulation setup

Figure 7 shows the setup used for the MD simulations. The setup consists of four components: the workpiece, the tool, the lubricant, and the external piston, which maintains a constant external pressure on the lubricant ($p = 0.6$ MPa). To investigate the impact of a nanocavity on the tool's surface concerning the squeeze-out of the lubricant, two case studies are presented: (i) a tool with a flat surface and (ii) a tool with a concave nanocavity. A simplified triangular-shaped tool was utilized. This simplification offers several advantages. First, a symmetric tool does not introduce artifacts by altering the lubricant flow pattern in a preferential direction, as any asymmetric effects are minimized or canceled out. This facilitates the analysis of lubrication effects, providing a clearer understanding of how lubricants behave during the machining process. Second, using a symmetric tool allows for easier control of external pressure by applying a piston to one face of the simulation box while maintaining periodic boundary conditions in the x and y directions, which ultimately reduces the number of lubricant molecules for a fully submerged tool.

The lubricant molecules are modeled as 1-decene trimer, which is the main component of 4 cSt polyalphaolefin (PAO4), a common paraffin-based oil in synthetic lubricants. The dimensions of the workpiece are 94 nm, 6.2 nm, and 23 nm in the x, y, and z directions, respectively. The simulation setups contain approximately 1.8 million atoms. To avoid the center-of-mass translation of the workpiece, five atomic layers are fixed at the bottom of the simulation box. Above the fixed layer, a thermostat layer is defined with a length of 5 atomic layers. The heat generated during the indentation process is removed by the Langevin thermostat applied to the thermostat layer. The time step was set to 1 fs. All MD simulations were conducted in LAMMPS [47]. A constant velocity in the z direction was used for the tool. Two velocities were studied: 2.5 m/s and 5 m/s. However, no differences were observed between the two velocities, so here only the results for the 5 m/s case are presented. A maximum indentation depth of 15 nm was specified. The position of the contact line of the lubricant was calculated by cluster analysis, using a distance-based criterion. Lubricant atoms that have a lower distance of 0.5 nm with respect to the tool and workpiece simultaneously are considered to be in the contact line cluster. The position of the contact line is calculated by taking the average position of the atoms in every contact line cluster. The position of the contact lines is calculated every 0.1 ns. The two-dimensional local pressure distribution in the xz plane was calculated using the atomic stress approximation, accounting for many-body interactions, such as bond, angle, and dihedral interactions [48].

3.4.2 Molecular models

The workpiece is modeled as a body-centered cubic (bcc) iron crystal with a lattice parameter of 2.86 Å. The workpiece

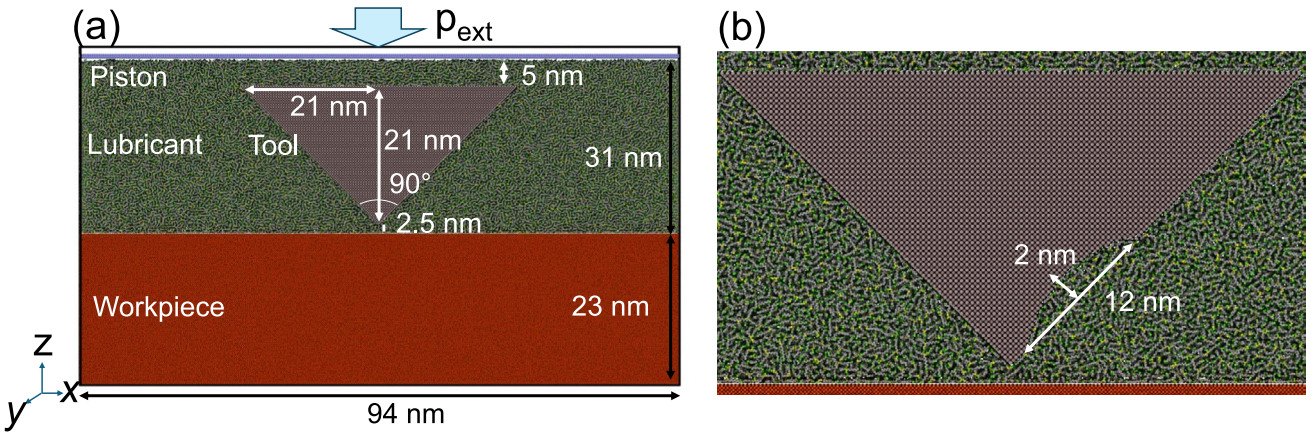

Fig. 7 (a) Setup for the MD simulations and (b) tool with nanoroughness

has the surface (100) exposed to the lubricant and the tool. Fe-Fe interactions are modeled by the interatomic potential modified embedded atom (MEAM) of Etesami et al. [49], and the lubricant-lubricant interactions by the united-atom force field by Potoff et al. [50]. The tool and the external piston are modeled as rigid bodies. The tool was modeled as a monoatomic bcc crystal, with a lattice parameter of 4.04 Å. The interactions between the tool and the workpiece are purely repulsive, i.e. modeled by a Weeks-Chandler-Anderson potential (WCA) [51], using the Lennard-Jones parameters of Heinz et al. for Fe [52] and Al [53]. The interactions of the tool and workpiece with the lubricant are represented by a 12-6 Lennard-Jones potential. The depth of the potential well (ϵ) in the Lennard-Jones potential was systematically adjusted to accurately fit the experimental work of adhesion, as previously suggested by [54]. The values of the fitted parameters and the details are given in Appendix C. The work of adhesion is calculated using the dry-wall method [55].

Like any model, the molecular setup and MD simulations presented here have certain limitations. To avoid generalization and misinterpretation of our findings, we briefly discuss some of these limitations. The most significant limitations are: the use of a sharp tool and a workpiece with a flat surface, the limited size of the tool nanocavity, the selection of a single crystal orientation, a unique chemical composition, and the examination of only one temperature.

Using a different tool geometry mainly affects plastic deformation behavior (see Ref. [56]), which is not the focus of this study. Sharp tools are commonly used in MD studies of machining processes; see, for instance, Ref. [57]. Despite the limited size of the tool cavity, relevant insight can be obtained about the lubricant squeeze and retention mechanism. This is possible because the key steps of those processes occur at a distance of a few molecular layers, and therefore, the size of the cavity becomes irrelevant. Investigating and optimizing larger cavities require combining MD with continuum models, which will be explored in future work.

We consider that the effects of crystal orientation on the squeeze process studied here are negligible. MD and DFT calculations of the adsorption energy of alkanes on Fe surfaces with different orientations reveal a variation of approximately 0.05 eV [58]. These are moderate differences compared to the mechanical work done by the tool on the lubricant during the squeezing process, which is 0.5 eV for 1 GPa and a displacement of 0.5 nm (typical interlayer distance). Therefore, we expect crystal orientation to have a minimal effect compared with the extreme mechanical conditions considered here. However, changes in the chemical composition of surfaces can significantly alter the adhesion forces, leading to different squeezing behavior. Due to the critical role of adhesion forces, the workpiece/lubricant and tool/lubricant interactions were adjusted to reproduce the experimental work of adhesion of the materials used in this study (see Appendix C). Finally, temperature effects can also change the squeezing behavior. For instance, higher surface temperatures weaken adsorption and reduce viscosity, facilitating the lubricant to squeeze out. However, thermal softening of the surface can promote molecular entrapment. Despite these limitations, the model still offers valuable insights into the mechanism of lubricant retention.

4 Results

4.1 Experimental results

The experiments were conducted using a 10-cut strategy with a centered infeed, and the offset between the tool and tooth centerlines was zero, as illustrated in Fig. 8. Each cut was performed with a constant cross-axis angle, and the corresponding feed s_{ax} (mm/workpiece rotation) are provided in Table 8.

Figure 9 shows the measurement results for the forces present in the process in comparison between dry machining and machining with oil flood cooling. Figure 9a shows the measured force values for the last depth of cut (TT10) as an exemplary case. The shaded area indicates the minimum and maximum deviations of the measured time sequences of the force. It is important to note that the force times of components x and y are measured in a rotating coordinate system. The diagram shows that the measured characteristic force curve is almost independent of the chosen cooling method. While the force curves for x and y are identical, a slight influence on the forces can be seen when considering the determined mean value of the z force. Thus, a reduction in the maximum force of 3% was determined by using oil. However, when the measured minimum and maximum values are taken into account, no significance can be identified due to their overlap. Figure 9b shows the maximum measured force values in the z direction (see Fig. 9a) for the depths of cut TT 1-10 in direct comparison of the different cooling methods under investigation. For TT 1-5 in particular, no influence on the maximum forces can be determined. Only from TT 6 to TT 10 a slight influence can be detected. However, this influence is at the same level as described in Fig. 9a and due to the range of error bars, the effect of the cooling lubricant cannot be proven.

In machining, chip morphology is a further important comparative parameter for evaluating the cooling lubrication method. Figure 10 shows the results for the chips measured in the CT. For a meaningful evaluation, the ratio of volume to surface area was analyzed. This value indicates

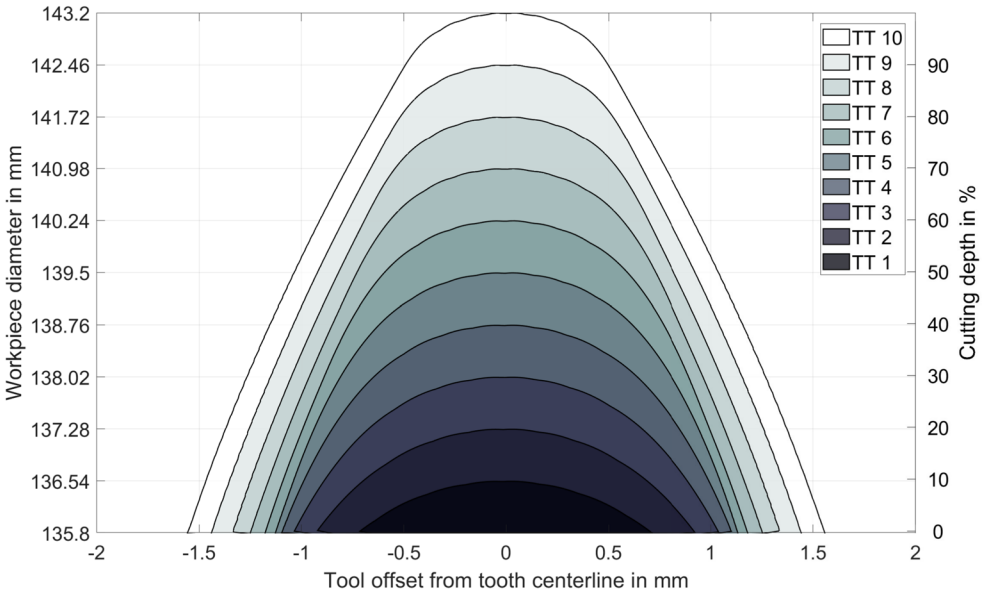

Fig. 8 Centered infeed strategy [27]

Table 8 Corresponding feed values for each cut according to the chosen cut strategy

TT	s_{ax}
	(mm/wr)
1	0.300
2	0.300
3	0.300
4	0.350
5	0.350
6	0.400
7	0.420
8	0.420
9	0.420
10	0.420

findings in the orthogonal cut, where the chip thickness is reduced by the use of cooling lubricant [59]. This finding also shows that not all findings from simplified chip formation can be transferred to complex processes.

4.2 FEM Results

Figure 11a shows the results of the TT-10 of the surface formation simulation in comparison to the experimentally determined data. This work focuses on cutting forces and chip formation, which are directly compared with experimental results. Other mechanical and thermal fields, such

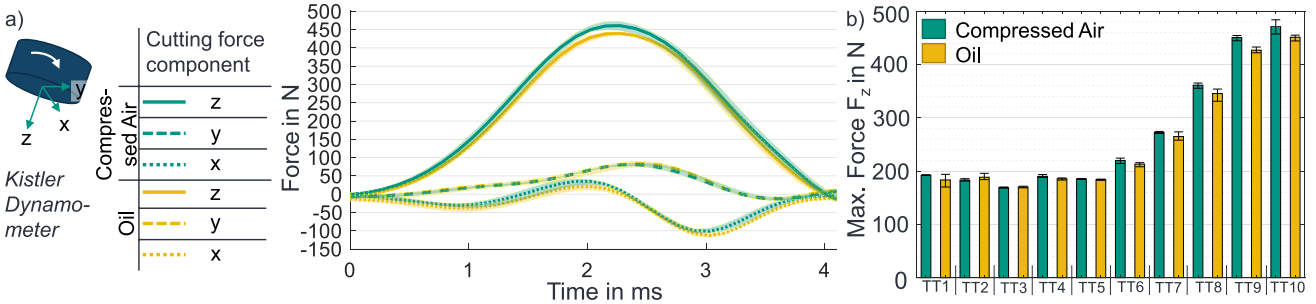

Fig. 9 (a) Comparison of measured forces with use of compressed air(green) and oil (yellow) during one tool engagement for the last infeed b) Comparison of maximum *z*-Forces with compressed air (green) and oil (yellow) for the 10 infeeds of the investigated process

the compactness of the analyzed chips, whereby the lower the coefficient, the more surface-heavy the analysis. It is evident that the ratio of V/A for the compressed air cooling method is always lower than for oil flooding in the gear skiving process analyzed. These results and the assumption of volume constancy indicate that the chip thickness tends to increase during chip formation when oil is used for gear skiving. These observations are in contradiction with as stress, strain rate, and temperature, are highly sensitive to input parameters (e.g., friction conditions and material models) and could not be reliably validated with the current experimental setup. As the model cannot yet provide testable predictions for these fields, they are not addressed in this study. Based on the findings of the tribological simulations, the mean value of the measured data is used and thus pure dry friction is taken into account in the

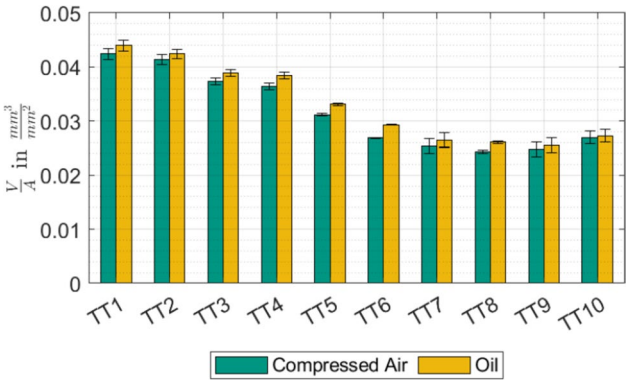

Fig. 10 Comparison of measured ratio of volume and area of chips with use of compressed air(green) and oil (yellow)

simulation. The simulation accurately predicts the initial cutting edge engagement, but it overestimates the maximum force in the *z*-direction. In contrast, the resultant force in the *xy*-plane is well reproduced by the simulation when compared to the experimental data. In analogy to the experimental study, Fig. 11b compares the determined maximum forces of the simulation with the mean values of the experimental study. It can be seen that the simulation can predict the maximum forces with an average error of 6.6%.

4.3 Validation of the SPH simulation of the global fluid distribution

For validation, the resulting oil particle distributions from the SPH simulations (cf. Section 3.2) are compared with the high-speed camera images from the experiments, as described in Section 2. Due to the highly transient and periodic nature of the process it is necessary to compare the same instant in physical time in the experiment and the simulation. Therefore, two characteristic frames are discussed based on configuration A. Configuration A is chosen because it provides the best optical access to the oil jet in the experiment, which is generally challenging to capture in high quality due to the high amounts of splashing oil in the system. In Fig. 12, an instant of time is shown where the oil jet flows nearly undisturbed from the top to the bottom of the image. The orientation of the tool, distinguishable by the tip of the cutting insert, is clearly the same in both the experimental and the simulated images. This situation is characteristic for the majority of the rotational cycle in the configuration A.

Only the tool tip and the protruding part of the workpiece are periodically impacted by the jet, once per revolution of the respective components. Taking a closer look at the experimental image, several droplets can be distinguished in the lower area of the frame. In contrast no droplets are visible in the same region in the simulated image. This can be explained by the fact that, in the experiment, the oil jet eventually hits the bottom plate of the chuck, where it impinges and partially disintegrates. Some of the rebounding droplets are captured by the camera. In the simulation, however, the particles are removed before they reach this bottom plate. The oil film and ligament stripping on the right-hand side of the workpiece, visible in the simulation image, are difficult to identify in the experimental image due to poor contrast and a limited field of view, which is obstructed by one of the jaws.

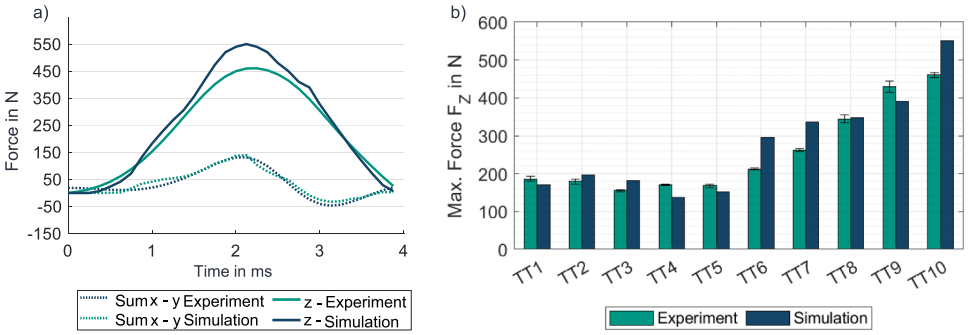

Fig. 11 (a) Comparison of simulated and experimental force profiles for TT-10 during final surface formation of gears. The resultant force in the *xy* plane shows good agreement with experimental data. b) Comparison of maximum cutting forces in *z*-axis from simulation and experimental measurements

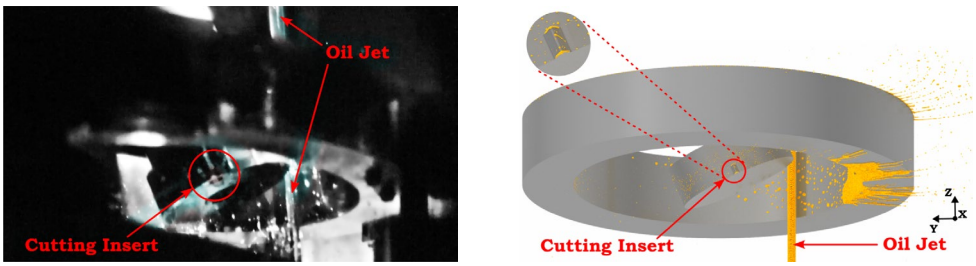

(a) (b)

Fig. 12 Oil distribution in configuration A, no interaction with the jet (a) Experiment (b) Simulation

In Fig. 13, the chosen time instant occurs shortly after the meshing zone, where the tool tip and the workpiece interact, interferes with the oil jet. Again, the orientation of the tool is consistent between the experiment and the simulation. Three main characteristic structures are highlighted in the figure. The clearly visible jet tip results from the interception of the previously undisturbed oil jet (shown in Fig. 12) by tool tip and the protruding part of the workpiece. Both components rotated into the jet shortly before the images were captured. The jet tip itself appears flattened, and a mushroom-shaped structure is stripped radially outward from the jet's central axis. The shape and size of this structure are very similar in both the simulation and the experiment.

Furthermore, a lamella, sheared off from the protruding part of the workpiece, is observable. The location and size of this structure in the simulation do not exactly match those of the experiment. Possible reasons include a slightly misaligned nozzle or the extremely thin nature of the lamella, making it difficult to discretize accurately. Finally, an oil film on the annular part of the workpiece, adjacent to the protrusion, can be observed in both the simulation and the experiment, although only upon closer inspection.

In summary, the characteristic and distinguishable features observed in the experimental images can also be identified from the simulation results. These observations hold for configurations B and C as well, although with the drawback of reduced optical access and increased oil splashing. Overall, the presented simulation methodology can be regarded as validated.

4.4 Wetting results from the SPH simulations

To address the central question of whether oil is fed into the meshing area where the tool and workpiece come into contact, a more detailed analysis of the simulation results is presented in the following section. By utilizing a wetting sensor, which detects oil particles in proximity to wall particles, the wetted regions of a rigid body surface can be easily identified. In Fig. 14, the wetting of the workpiece near the tooth gap is depicted at the instant when the tool tip and workpiece begin to mesh. With the binary color bar, red areas indicate wetted regions, while blue areas denote dry regions. In all three investigated configurations, the tooth gap is covered by an oil film. Naturally, the detailed distribution of wetted areas depends on the position of oil jet injection relative to the meshing zone. As a result, the distribution varies across the three configurations.

The same approach is used for Fig. 15, which depicts the wetting of the tool tip's rake face at the instant when the tool tip and workpiece begin to mesh. Despite minor differences, the wetting distribution appears very similar for all three configurations. Essentially, the entire area of the rake face is wetted.

In conclusion, for all investigated nozzle configurations, global oil distribution simulations predict that oil is indeed fed into the meshing region, both on the tool tip and within the tooth gap of the workpiece. The pressure in these oil films is approximately equal to ambient pressure, as there is no direct impact from the oil jet. These global fluid distribution simulations neglect the chip and its formation as stated in Section 3.2.2. Investigations on smaller scales, including the influence of chip formation by means of Reynolds calculations and MD simulations, are presented in the following sections. The obtained results (oil is present at ambient pressure in the beginning of the chip formation) from these global fluid distribution simulations provide the initial condition for the Reynolds calculations which are presented in the next section.

4.5 Reynolds calculations

Figure 16a shows the relationship between chip velocity and dry contact length L_{dry} in the contact wedge calculated by the Reynolds lubrication equation. The dry contact length L_{dry} increases with the chip velocity, indicating that higher speeds promote cavitation and reduce lubricant penetration

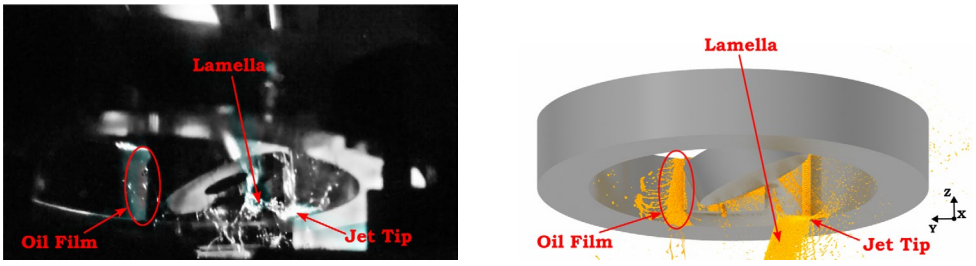

Fig. 13 Oil distribution in configuration A, shortly after interaction with the jet (a) Experiment (b) Simulation

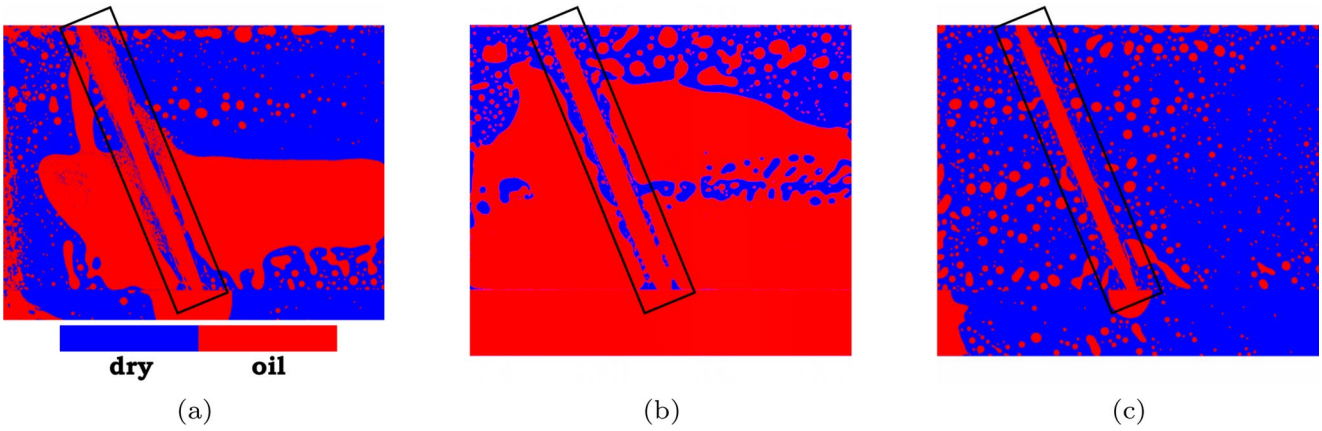

Fig. 14 Wetting of the tooth gap in the beginning of the meshing (a) configuration A, (b) configuration B, and (c) configuration C

Fig. 15 Wetting of the cutting insert in the beginning of the meshing (a) configuration A (b) configuration B (c) configuration C

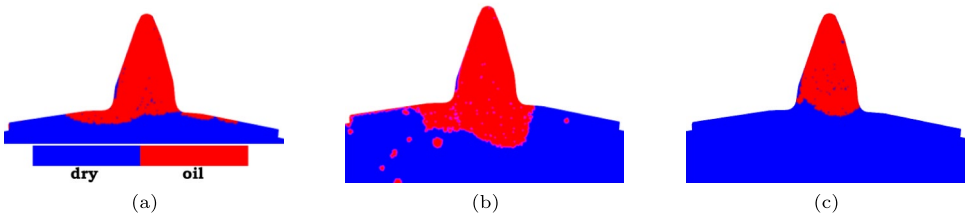

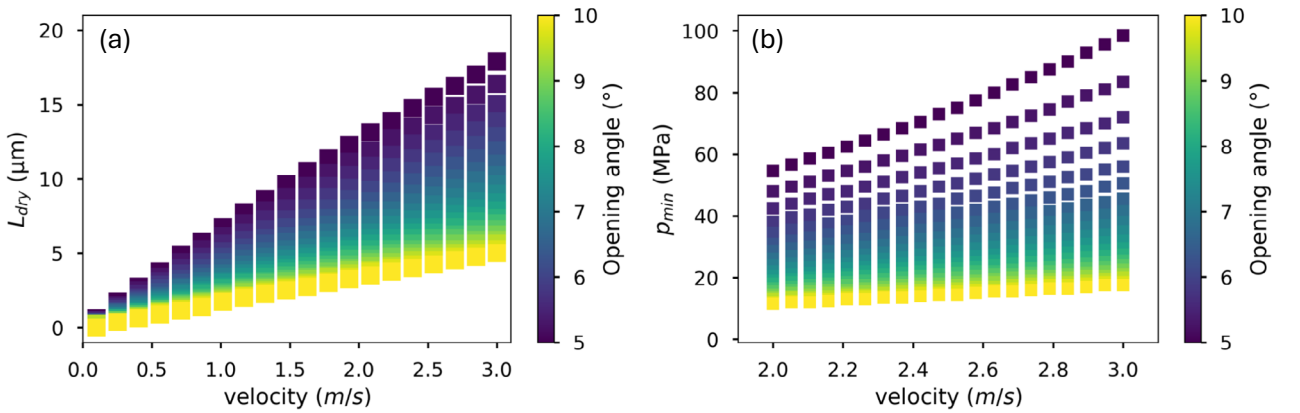

Fig. 16 (a) Dry length as a function of the chip velocity and opening angle. (b) Minimum pressure for reaching full lubrication as a function of the chip velocity and opening angle

within the contact zone. In addition, the opening angle significantly changes the extent of cavitation. Larger opening angles consistently result in shorter dry lengths, suggesting improved lubricant penetration. Conversely, smaller angles increase cavitation, especially at higher velocities.

Under typical gear skiving conditions, i.e., chip velocities between 1.8 and 2.5 *m*/*s* and opening angles ranging from 5° to 10°, our calculation indicates that the tool contact region is partially cavitated rather than fully lubricated. At these chip velocities, L_{dry} spans a significant range, increasing with lower opening angles. For example, at 2.5 *m*/*s* and 5°, the dry length exceeds 15 μm, suggesting substantial lubricant depletion. Even at the more favorable 10°, a non-negligible L_{dry} of around $5-7$ μm persists. This implies that under these conditions, the tool does not remain fully wetted and operates within a mixed lubrication regime, where cavitation and dry contact are present. Large cavitated areas reduce the effective load-bearing surface within the contact zone, concentrating mechanical loads on a smaller region. This concentration increases local stresses and can accelerate tool wear and deformation along the rake face and cutting edge. Recently, Denkena et al. [60] observed that during lubricated machining of AISI4140, cutting and

passive forces remained largely unaffected by the lubricant supply pressure. However, friction in the secondary zone significantly decreases as lubricant supply pressure increases. These results align well with our findings and suggest that increasing the lubricant supply pressure may help reduce the length of the cavitated area.

For the present Reynolds model and gear skiving conditions, it is possible to determine the minimum pressure that leads to a full lubrication film in the cutting wedge. This pressure, p_{min}, was defined as the lowest pressure for which no cavitation exists for all N nodes in the domain, i.e. $p_{\min} = \min\{p : \theta_i(p) = 0, \ \forall i \in \{1, \ldots, N\}\}$. The pressure p_{min} was determined by systematically increasing pressure on the right side of the wedge using a step of 0.5 MPa.

Figure 16b shows p_{min} as a function of the chip velocity and opening angle. The results indicate that p_{min} increases with both the chip velocity and the decreasing opening angle. At higher velocities, the lubricant must overcome greater inertial and shear effects to maintain film continuity, thus requiring higher supply pressure. In contrast, a smaller opening angle increases p_{min}, which implies that it facilitates cavitation. This analysis provides a quantitative guideline for setting minimum lubricant pressures in high-speed skiving operations. Notably, it highlights that for standard gear skiving velocities (2.0–2.5 *m*/*s*), full lubrication is only feasible for larger opening angles unless high pressures are applied. This potentially explains why the effects of lubricants are limited in practice and cavitation persists under typical cutting conditions.

The Reynolds model presented here provides a valuable first-order approximation of the hydrodynamic behavior in lubricant flow and cavitation that occurs across the cutting wedge during gear skiving. It effectively highlights key trends in cavitation and serves as a solid baseline for understanding lubrication in the complex gear-skiving process. Given the micrometer-scale film thickness considered, certain effects, such as wall slip and shear rate, can be safely neglected, as they only become significant at nanometer-scale film thicknesses. While the model is based on simplifying assumptions, these assumptions allow for a focused and manageable analysis of the dominant mechanisms involved. Future refinements could include incorporating additional physical phenomena such as thermal gradients, transient chip formation, surface roughness, and capillary effects. Addressing these phenomena would require establishing appropriate constitutive relations for each mechanism, including models for temperature-dependent viscosity, temperature-dependent thermal conductivities, and the dynamic behavior of the contact angle. Developing and integrating such models will be an important direction for future research, although it is beyond the scope of the present study.

Among the physical mechanisms excluded from our Reynolds model, the roughness of the tool surface plays a particularly important role in shaping the local pressure field and influencing lubricant retention [61, 62]. Roughness-induced effects are known to disrupt the smooth flow predicted by classical lubrication theory, introducing local pressure fluctuations and modifying the distribution of the fluid film. This is especially relevant during the initial approach between the tool and the workpiece when the fluid is first displaced or confined by surface cavities. To investigate this in more detail, we conduct MD simulations of the indentation step, focusing on how roughness at the nanoscale affects lubricant retention in the early stages of contact formation.

4.6 Molecular simulations

Figure 17a shows the position of the contact line for both the flat surface and the tool with the nanocavity. In the case of the flat surface, the contact line moves in the *x*-direction on average at 5.2 *m*/*s*, which is close to the velocity imposed on the tool. As Fig. 17b shows, no lubricant molecule gets trapped in the contact area. This means that the tool surface remains dry as it penetrates deeper into the workpiece, resulting in a complete squeeze-out of the lubricant. In contrast, for the nanostructured tool surface, the contact line velocity decreases, allowing some lubricant molecules to trail behind the tool. Figure 17b shows that for the tool with nanoroughness, a few molecules enter the contact area.

Figure 18a and b provide a snapshot after the tool has advanced 10 nm into the workpiece. The tool with nanoroughness, where a few molecules form a submonolayer, parially prevents direct contact between the tool and the workpiece.

The enhancement of the retention of lubricant molecules on nanostructured surfaces can be explained by several mechanisms. An important mechanism is the increase in surface area that the contact line must navigate as the tool advances. The nanoroughness alters the contact mechanics between the cutting tool and the workpiece, slowing the squeezing process and creating more opportunities for lubricant molecules to become trapped in the contact area. Furthermore, surface roughness significantly increases the local normal pressure component,

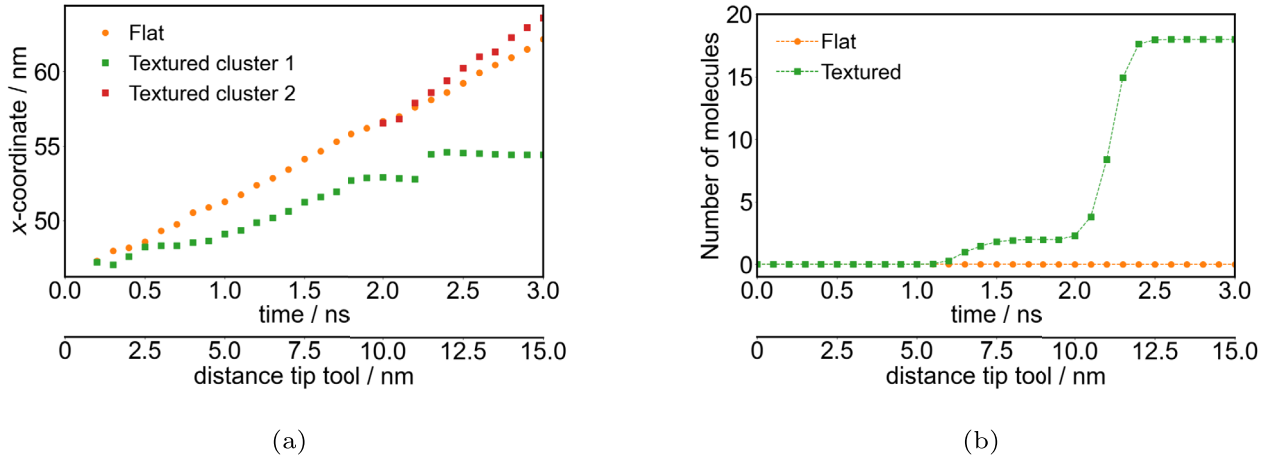

Fig. 17 (a) Position of the contact line in the x direction as a function of time and (b) number of lubricant molecules trapped in the direct chip-tool contact area (i.e. $z < 23$nm) as a function of time

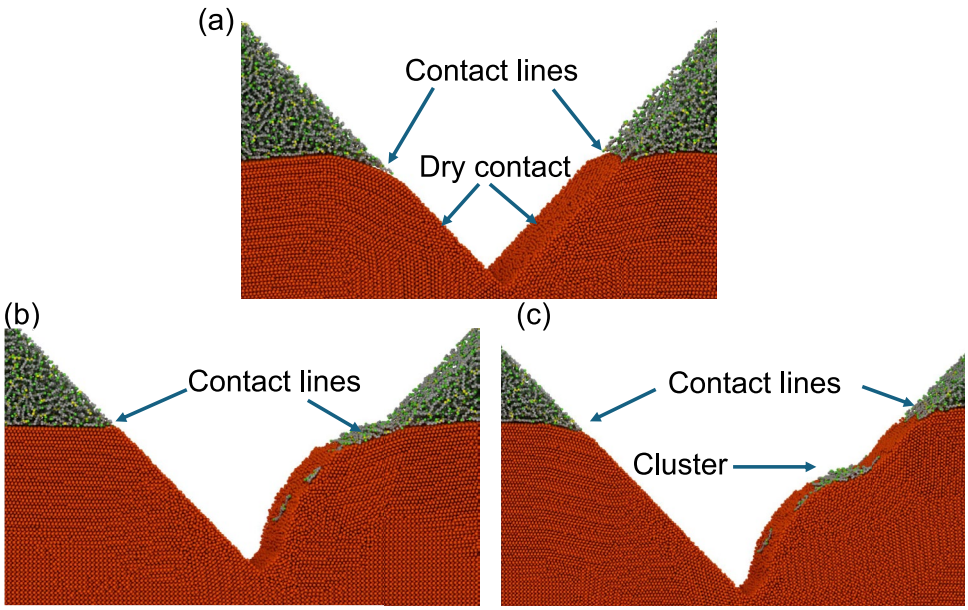

Fig. 18 Snapshots of the MD simulations: (a) flat surface at $t = 2ns$ (10 nm indentation distance), (b) tool with nanoroughness at $t = 2ns$ (10 nm indentation distance), and (c) tool with nanoroughness $t = 2.5ns$ (12.5 nm indentation distance)

reaching values close to 1 GPa (see Fig. 19). This leads to local deformation of the workpiece, further enhancing the retention of lubricant molecules. These mechanisms are geometric and mechanical. Moreover, the surface adsorption alteration can also play a role. Concave surfaces exhibit adsorption energy higher than that of flat surfaces. The strengthened interactions can, for instance, reduce the lubricant wall slip. The relative importance of these mechanisms is intricate, and quantifying them is beyond the scope of this paper.

5 Conclusions

The findings of this study provide insights into the key questions regarding lubricant behavior in gear skiving operations:

1. **Effect of lubricant on cutting forces:** Experimental results indicate that the use of oil flood cooling in gear skiving has a limited impact on the mechanical forces involved in the process. Force measurements show

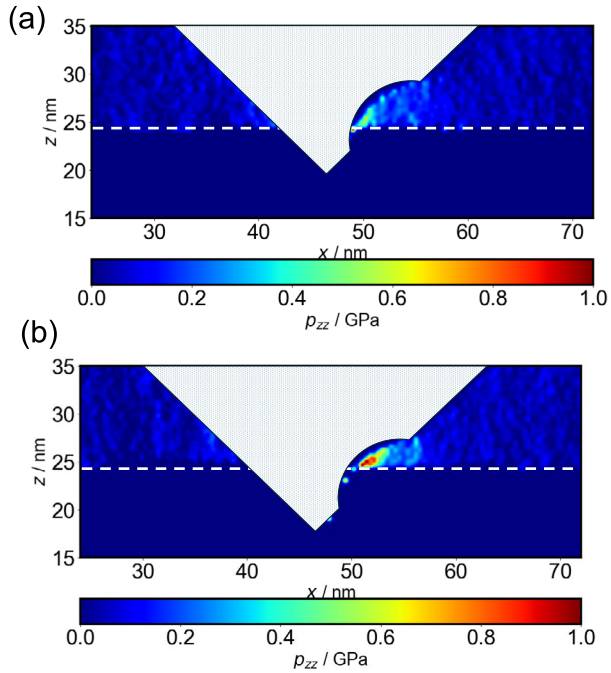

Fig. 19 2D distribution of the normal component of pressure p_{zz} from MD simulations for the tool with nanoroughness at: (a) t = 1 *ns* and (b) 1.5 *ns*

no significant differences between dry and lubricated conditions in the x and y directions. There is only a marginal and statistically insignificant reduction in the z-direction forces with oil lubrication. Furthermore, chip morphology analysis reveals that lubrication results in slightly thicker chips, as indicated by a higher volume-to-surface-area ratio. This observation contrasts with findings from simplified orthogonal cutting, emphasizing the need for a process-specific understanding of lubrication behavior in complex machining operations.

2. **Global lubricant delivery:** The SPH simulations demonstrate that the cooling lubricant can effectively reach the meshing zone between the tool and workpiece during gear skiving. The cooling strategy employed directs the oil to this critical region, ensuring that both the tool's rake face and the workpiece are initially covered with an oil film during the meshing process.
3. **Local penetration mechanisms:** The penetration of the lubricant into the cutting wedge is influenced by several factors, including chip velocities and the tool-chip opening angle. The occurrence of cavitation is common under the studied operational conditions, especially when high chip velocities and narrow opening angles are present, which can impede adequate lubrication.
4. **Molecular-scale transport:** The surface topography of the tool plays a significant role in the transport of lubricant molecules. Specifically, nanocavities on the tool surface enhance lubricant retention by increasing local normal pressure, thereby trapping the lubricant in the contact regions and preventing its complete squeeze-out during machining.
5. **Process optimization:** The interplay between chip velocity, coolant pressure, and the chip-tool opening angle is critical for minimizing dry contact zones. To maximize lubricant penetration at the tool-chip interface, it is essential to optimize these parameters effectively. The findings suggest that higher coolant pressures combined with process parameters that ensure wider opening angles can significantly enhance lubrication reliability and performance in high-speed gear manufacturing.

Overall, this study emphasizes the importance of integrating strategies related to lubricant delivery, penetration mechanisms, molecular transport, and process parameters to enhance lubrication effectiveness in industrial skiving processes.

6 Supplementary information

No information is required.

Appendix A Microstructure of AISI 4140 Workpiece Material

Figure 20 shows the typical microstructure of the AISI 4140 workpiece material following quenching and tempering at 600 °C for one hour. This image was captured using a Keyence VHX-7000 digital microscope at 1000× magnification. The microstructure predominantly consists of tempered martensite characterised by fine, lath-like features arranged in packets, which indicates a successful heat treatment process.

Appendix B Pressure-viscosity constitutive relation for the Reynolds calculation from MD simulations

The viscosity of the lubricant was determined using non-equilibrium molecular dynamics (NEMD), employing methods similar to those described by Jadhao et al. [63]. The lubricant consisted of pure 1-decene trimer molecules, which were modeled using the Potoff potential [50], as this

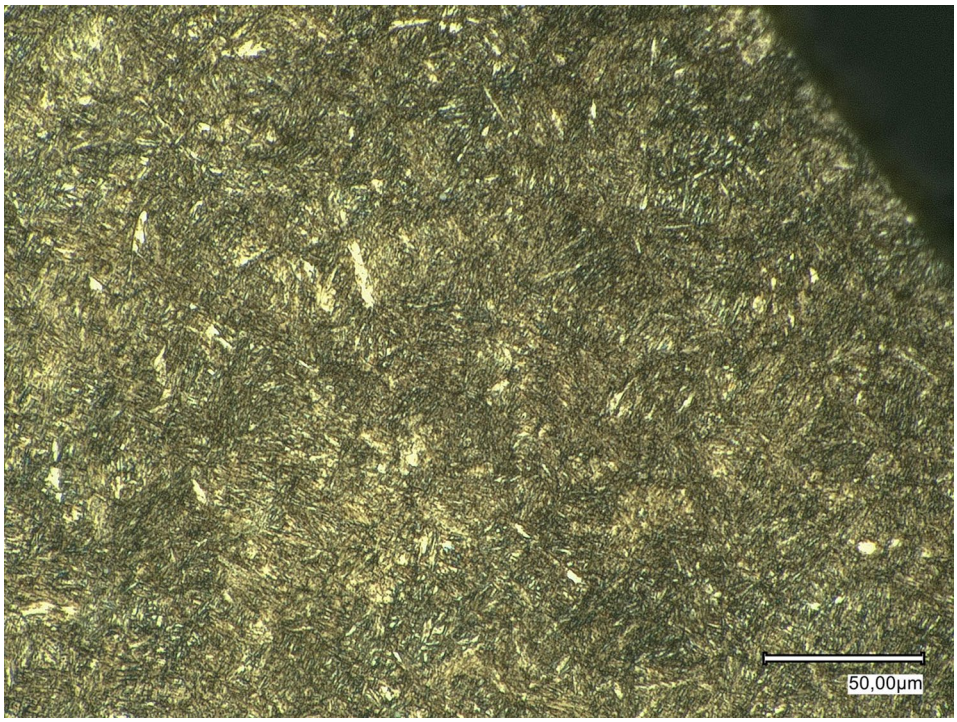

Fig. 20 Hardened microstructure of initially austenitized AISI 4140 steel at 600°C for one hour according to DIN EN ISO 18265

potential has been suggested to accurately represent the transport properties of long paraffinic molecules [64]. A cut-off radius of 1.2 nm was established, and periodic boundary conditions were applied in all directions. The time step for the simulations was set to 1 fs.

Before conducting the NEMD simulations, the system was equilibrated to achieve the target pressure and temperature. A total of 125 molecules were used. The effect of using a larger system was investigated, and it was found that increasing the number of molecules to 216 or 343 did not have a significant impact on the calculated viscosity.

The system was first equilibrated in a low-viscosity state at a temperature of 373.15 K and a pressure of 0.1 MPa using a Nosé–Hoover thermostat and barostat for a duration of 40 ns. Following this, the size of the simulation box was dynamically adjusted to match the average density obtained from the NPT simulation. This adjustment of the box size was conducted over a period of 10 ns, utilizing a Langevin thermostat to maintain a constant temperature. The final state of this simulation was then used as the initial state for the NEMD simulations and the equilibration of the next higher target pressure.

NEMD simulations were performed at constant density and temperature. A shear rate was applied to the simulation box using the SLLOD method [65]. Each NEMD simulation was conducted for 40 ns, with the initial 20 ns discarded to allow the system to reach steady state. Shear stress was saved every 1000 time steps. The steady-state shear stress

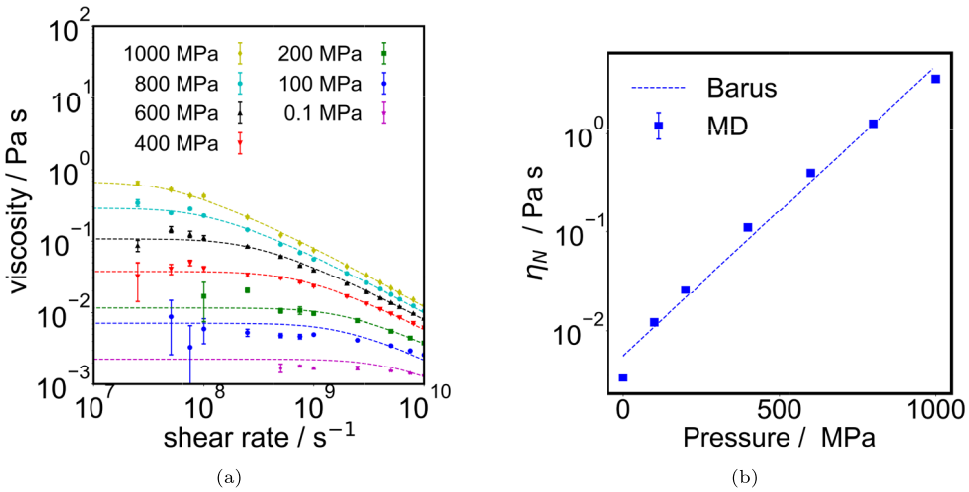

Fig. 21 (a) Viscosity of the lubricant (1-decene trimer, PAO4) as a function of the shear rate calculated using NEMD at 373.15 K. The dashed lines are the fitting using the Eyring model. (b) Newtonian viscosity as a function of the pressure. The dashed line is the fitting using the Barus model

was calculated by averaging the last 20 ns of the simulation. To assess the uncertainty in the shear stress, a block averaging method was utilized, dividing the data into 10 blocks. Figure 21a shows the calculated viscosities as a function of the shear rate.

Newtonian viscosities (η_N) were determined using the linear relationship between the shear stress and the logarithm of the shear rate ($\dot{\gamma}$), as described in [63], ie $\tau = \tau_E \ln[2\dot{\gamma}(\eta_N/\tau_E)]$, where τ_E is the Eyring stress. This equation is an approximation of the Eyring model for the large shear rate, where $\tau >> \tau_E$ is expected. Figure 21b shows η_N as a function of pressure. The dependence of the Newtonian viscosity on pressure was modeled by the Barus equation:

$$\eta_N = \eta_0 e^{\alpha p} \tag{A1}$$

The fitting parameters were $\eta_0 = 5.562 \times 10^{-3}$ Pa s, and $\alpha = 6.763 \times 10^{-9}$ Pa^{-1}

Under the conditions used for Reynolds calculations ($p < 200$ MPa and $T = 373.15$ K), the lubricant shows significant shear thinning at shear rates exceeding 1×10^9 s^{-1} (see Fig. 21a). For the maximum velocity used in the Reynolds model (3 m/s), a shear rate of 1×10^9 s^{-1} is only reached when the film height is less than 3 nm. In the first node on the left side of the Reynolds geometry (see Fig. 6), the height of the wedge for the smallest opening angle considered (5°) is approximately 10.94 nm. Therefore, we decided to neglect the effects of shear thinning and assumed that the lubricant behaves as a Newtonian fluid.

Appendix C Fitting of the workpiece/lubricant and tool/lubricant interaction parameters

A key element of MD simulations is to have a reasonable representation of the lubricant/tool and lubricant/workpiece interactions. As suggested by Carman et al. [54], the work of adhesion (W_{sl}) is a suitable property to characterize and adjust such interphase interactions. The work of adhesion is the reversible work per unit area required to separate two interfaces, and it can easily be obtained from experiments and MD simulations. The work of adhesion is related to the contact angle (θ) and the liquid-vapor surface tension (γ_{lv}) by the following equation:

$$W_{sl} = \gamma_{lv}(1 + \cos\theta) \tag{A2}$$

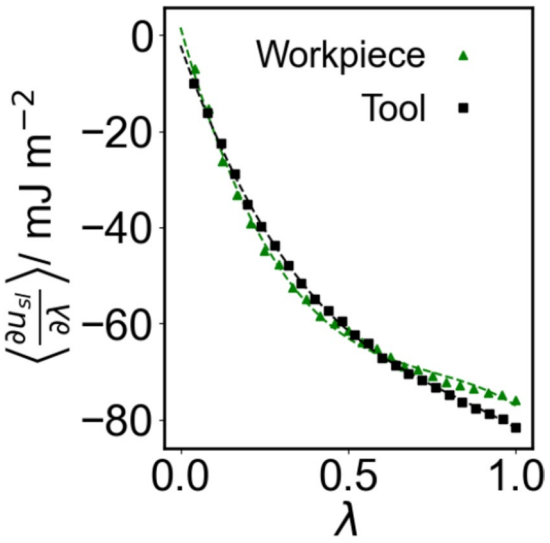

Fig. 22 Derivative $\left\langle \frac{\partial u_{sl}}{\partial \lambda} \right\rangle$ as a function of the coupling parameter λ for the refitted $\epsilon_{solid-lubricant}$ interactions. Dashed lines represent fitting curves obtained through a third-degree polynomial regression

On the other hand, W_{sl} can be obtained from MD simulations by using the dry-wall method [55] by applying the following equation:

$$W_{sl} = -\int_0^1 \left\langle \frac{\partial u_{sl}}{\partial \lambda} \right\rangle \mathrm{d}\lambda \tag{A3}$$

where u_{sl} is the solid-lubricant potential energy per unit of area and λ is the coupling parameter. For $\lambda \approx 0$, the lubricant is decoupled from the surface. For $\lambda = 1$, the lubricant interacts fully with the surface.

The experimental liquid-vapor surface tension for PAO4 and the static contact angle between PAO4 and steel were taken from Ref. [66]. The experimental γ_{lv} was 29.01 *mN/m*, which is similar to that reported here for the complex lubricant Fuchs Ecocut 715 LE (29.0 *mN/m*, see Table 7). The experimental static contact angle between PAO4 and the workpiece surface (steel) was 10.9°, indicating good wettability, as confirmed by our dynamic contact angle measurements (Table 7). Applying Eq. A2, the experimental lubricant/workpiece work of adhesion is 57.49 mJ/m^2.

Table 9 LJ parameters for the tool/lubricant and WP/lubricant interactions

interaction	σ	ϵ
	(Å)	(*eV*)
Fe (WP)	2.59[a]	0.0150
Al (Tool)	2.925[b]	0.01352

[a] from [52]. [b] from [53]

The contact angle between the tool and the lubricant could not be measured due to the dimensions and geometry of the tools used in this study. Unfortunately, no experimental data are available for the AlCrN/oil contact angle in the literature. However, studies on similar materials suggest high hydrophobicity and oleophilic behavior. For example, AlN has been shown to exhibit superhydrophobic behavior [67]. In addition, the experimental water/AlCrN contact angle is approximately 85°, which is higher than the water/steel-ANSI4340 contact angle (78°) [68]. The surface energy of AlCrN coatings is 28-42 mJ/m^2 [68, 69], which is similar to that of oleophilic materials such as ta-C (48.58 mJ/m^2). [66] Additionally, Wróblewski [70] reported a contact angle of 20.6° for an AlN/CrN/.../AlN/CrN multilayer nanocoating and oil. Based on this, we adopted a contact angle of 20.6° for the tool/lubricant, leading to a reference experimental W_{sl} of 56.16 *mJ/m*.

To calculate W_{sl} from MD, we conducted simulations for 25 coupling parameters λ in the domain $\lambda \in (0, 1]$. The potential energy u_{sl} and the derivative $\frac{\partial u_{sl}}{\partial \lambda}$ were calculated every 100 time steps. For each λ, 0.25 ns was used for equilibration and 0.75 ns for production.

Applying the Lennard-Jones parameters of Heinz et al. [52] and the Lorentz-Berthelot mixing rules results in an overestimation of W_{sl}. The value of ϵ in the LJ potential was systematically decreased. Figure 22 shows that $\left\langle \frac{\partial u_{sl}}{\partial \lambda} \right\rangle$ for the values of ϵ closely reproduce the experimental W_{sl}. Table 9 gives the final LJ parameter for the tool and WP. Crossed LJ parameters for tool/lubricant and WP/lubricant interactions calculated using Lorentz-Berthelot mixing rules.

Acknowledgements The research was generously funded by the DFG ("Deutsche Forschungsgemeinschaft") under the project "FluSimPro" (439954775). The authors gratefully acknowledge the computing time provided on the high-performance computer HoreKa by the National High-Performance Computing Center at KIT (NHR@KIT). This center is jointly supported by the Federal Ministry of Education and Research and the Ministry of Science, Research and the Arts of Baden-Württemberg, as part of the National High-Performance Computing (NHR) joint funding program (https://www.nhr-verein.de/en/our-partners). HoreKa is partly funded by the German Research Foundation (DFG).

Author Contributions — Conceptualization: Florian Sauer, Edder J. Garcia, Matthias Haber — Methodology: Florian Sauer, Edder J. Garcia, Matthias Haber — Software: Florian Sauer, Edder J. Garcia, Matthias Haber — Validation: Florian Sauer — Formal analysis: Florian Sauer, Edder J. Garcia, Matthias Haber, Amartya Mukherjee — Investigation: Florian Sauer, Edder J. Garcia, Matthias Haber, Amartya Mukherjee — Resources: Hans-Jörg Bauer, Michael Moseler, Volker Schulze — Data Curation: Florian Sauer, Edder J. Garcia, Matthias Haber — Writing (Original Draft): Florian Sauer, Edder J. Garcia, Matthias Haber, Amartya Mukherjee — Writing (Review & Editing):Florian Sauer, Edder J. Garcia, Matthias Haber, Amartya Mukherjee, Kerstin Falk, Corina Schwitzke, Hans-Jörg Bauer, Michael Moseler, Volker Schulze — Visualization: Florian Sauer, Edder J. Garcia, Matthias Haber, Amartya Mukherjee — Supervision: Kerstin Falk, Corina Schwitzke, Hans-Jörg Bauer, Michael Moseler, Volker Schulze — Project administration: Hans-Jörg Bauer, Michael Moseler, Volker Schulze — Funding acquisition: Hans-Jörg Bauer, Michael Moseler, Volker Schulze

Funding Open Access funding enabled and organized by Projekt DEAL.

Data Availability No datasets were generated or analysed during the current study.

Declarations

Competing interests The authors declare no competing interests.

References

1. Diba F, Naser J, Stephens G, Rahman Rashid RA, Palanisamy S (2024) Numerical study of coolant flow phenomena and heat transfer at the cutting-edge of twist drill. Appl Sci 14:5450. https://doi.org/10.3390/app14135450
2. Fernandes GHN, Ferreira ER, França PHP, Barbosa LMQ, Filho EB, Martins PS, Machado ÁR (2024) Internally cooled tools as an innovative solution for sustainable machining: temperature investigation using inconel 718 superalloy. CIRP J Manuf Sci Technol 50:269–284. https://doi.org/10.1016/j.cirpj.2024.03.001
3. Yan P, Rong Y, Wang G (2016) The effect of cutting fluids applied in metal cutting process. Proc Inst Mech Eng Part B 230:19–37. https://doi.org/10.1177/0954405415590993
4. Rakić R, Rakić Z (2002) Tribological aspects of the choice of metalworking fluid in cutting processes. J Mater Process Technol 124:25–31. https://doi.org/10.1016/S0924-0136(01)01150-5
5. Trent EM (1984) Metal Cutting, 2nd edn. Butterworths, London
6. Senthil Kumar A, Rahman M, Ng SL (2002) Effect of high-pressure coolant on machining performance. Int J Adv Manuf Technol 20:83–91. https://doi.org/10.1007/s001700200128
7. Sørby K, Tønnessen K (2006) High-pressure cooling of face-grooving operations in ti6al4v. Proc Inst Mech Eng Part B 220:1621–1627. https://doi.org/10.1243/09544054JEM474
8. Senevirathne SWMAI, Punchihewa HKG (2017) Comparison of Tool Life and Surface Roughness with MQL, Flood Cooling, and Dry Cutting Conditions with P20 and D2 Steel. In: IOP Conf. Ser. Mater. Sci. Eng., vol 244, pp 012006. https://doi.org/10.1088/1757-899X/244/1/012006
9. Devillez A, Le Coz G, Dominiak S, Dudzinski D (2011) Dry machining of inconel 718, workpiece surface integrity. J Mater Process Technol 211:1590–1598. https://doi.org/10.1016/j.jmatprotec.2011.04.011

10. Faga MG, Priarone PC, Robiglio M, Settineri L, Tebaldo V (2017) Technological and sustainability implications of dry, near-dry, and wet turning of ti-6al-4v alloy. Int J Precis Eng Manuf-Green Technol 4:129–139. https://doi.org/10.1007/s40684-017-0016-z
11. Klocke F, Krämer A, Sangermann H, Lung D (2012) Thermo-mechanical tool load during high performance cutting of hard-to-cut materials. Procedia CIRP 1:295–300. https://doi.org/10.1016/j.procir.2012.04.053
12. Stanford M, Lister PM, Morgan C, Kibble KA (2009) Investigation into the use of gaseous and liquid nitrogen as a cutting fluid when turning bs 970–80a15 (en32b) plain carbon steel using wc–co uncoated tooling. J Mater Process Technol 209:961–972. https://doi.org/10.1016/j.jmatprotec.2008.03.003
13. Stadtfeld HJ (2014) Power skiving of cylindrical gears on different machine platforms. Gear Technol 31:52–62
14. Arndt T, Klose J, Gerstenmeyer M, Schulze V (2022) Tool wear development in gear skiving process of quenched and tempered internal gears. Forsch Im Ingenieurwes 86:587–594. https://doi.org/10.1007/s10010-021-00544-0
15. Daniel D, Vuckovac M, Backholm M, Latikka M, Karyappa R, Koh XQ, Timonen JVI, Tomczak N, Ras RHA (2023) Probing surface wetting across multiple force, length and time scales. Commun Phys 6:1–15. https://doi.org/10.1038/s42005-023-01268-z
16. Williams JA, Tabor D (1977) The role of lubricants in machining. Wear 43:275–292. https://doi.org/10.1016/0043-1648(77)90125-9
17. Sauer F, Codrignani A, Haber M, Falk K, Mayrhofer L, Schwitzke C, Moseler M, Bauer H-J, Schulze V (2023) Multiscale simulation approach to predict the penetration depth of oil between chip and tool during orthogonal cutting of aisi 4140. Procedia CIRP 117:426–431. https://doi.org/10.1016/j.procir.2023.03.072
18. Muthusamy S, Arulmurugu A (2017) Computational of orthogonal metal cutting process using smooth particle hydrodynamics. Appl Mech Mater 867:119–126. https://doi.org/10.4028/www.scientific.net/AMM.867.119
19. Takabi B, Tajdari M, Tai BL (2017) Numerical study of smoothed particle hydrodynamics method in orthogonal cutting simulations – effects of damage criteria and particle density. J Manuf Process 30:523–531. https://doi.org/10.1016/j.jmapro.2017.10.020
20. Woloszynski T, Podsiadlo P, Stachowiak GW (2015) Efficient solution to the cavitation problem in hydrodynamic lubrication. Tribol Lett 58:1–11. https://doi.org/10.1007/s11249-015-0487-4
21. Alder BJ, Wainwright TE (1959) Studies in molecular dynamics. i. general method. J Chem Phys 31:459–466. https://doi.org/10.1063/1.1730376
22. Belak JF, Stowers IF (1990) A molecular dynamics model of the orthogonal cutting process. Technical Report UCRL-102697; CONF-9009241-1, Lawrence Livermore National Lab., CA (USA)
23. Belak J, Stowers IF (1992) The indentation and scraping of a metal surface: A molecular dynamics study. In: Singer IL, Pollock HM (eds) Fundamentals of Friction: Macroscopic and Microscopic Processes, pp 511–520. Springer, ???. https://doi.org/10.1007/978-94-011-2811-7_25
24. Sun X, Chen S, Cheng K, Huo D, Chu W (2006) Multiscale simulation on nanometric cutting of single crystal copper. Proc Inst Mech Eng Part B 220:1217–1222. https://doi.org/10.1243/09544054JEM540SC
25. Holey H, Sauer F, Ganta PB, Mayrhofer L, Dienwiebel M, Schulze V, Moseler M (2024) Multiscale parametrization of a friction model for metal cutting using contact mechanics, atomistic simulations, and experiments. Tribol Lett 72:113. https://doi.org/10.1007/s11249-024-01906-9
26. CloudCompare Development Team (2021) CloudCompare (version 2.10.3) [GPL software]. http://www.cloudcompare.org. Accessed: 2025-01-23
27. KIT Campus Transfer GmbH (2022) OpenSkiving. [Software]. Karlsruhe
28. Sauer F, Mukherjee A, Schulze V (2025) Insights into the metal cutting contact zone through automation and multivariate regression modelling under the framework of gear skiving. Simul Model Pract Theory 142:103107. https://doi.org/10.1016/j.simpat.2025.103107
29. Johnson GR, Cook WH (1985) Fracture characteristics of three metals subjected to various strains, strain rates, temperatures and pressures. Eng Fract Mech 21(1):31–48. https://doi.org/10.1016/0013-7944(85)90052-9
30. Richter F (2015) Die Physikalischen Eigenschaften Der Stähle - Das 100-Stähle-Programm. Tafeln Und Bilder, Teil I
31. Agmell M, Ahadi A, Ståhl J-E (2011) A fully coupled thermomechanical two-dimensional simulation model for orthogonal cutting: formulation and simulation. Proceed Inst Mech Eng Part B J Eng Manuf 225(10):1735–1745. https://doi.org/10.1177/0954405411407137
32. Sarmiento GS, Bugna JF, Canale LCF, Riofano RMM, Mesquita RA, Totten GE, Canale AC (2007) Modeling quenching performance by the kuyucak method. Mater Sci Eng, A 459(1):383–389. https://doi.org/10.1016/j.msea.2007.01.025
33. Kops L, Arenson M (1999) Determination of convective cooling conditions in turning. CIRP Ann 48(1):47–52. https://doi.org/10.1016/S0007-8506(07)63129-1
34. Keller MC, Braun S, Wieth L, Chaussonnet G, Dauch TF, Koch R, Schwitzke C, Bauer H-J (2019) Smoothed particle hydrodynamics simulation of oil-jet gear interaction. J Tribol 141(7):071703. https://doi.org/10.1115/1.4043640
35. Haber M, Schwitzke C, Bauer H-J (2023) Oil-jet lubrication of epicyclic gear trains. In: Proceedings of the 17th international SPHERIC workshop. Ed.: G. Fourtakas, pp 341–347. https://doi.org/10.5445/IR/1000169462
36. Lucy LB (1977) A numerical approach to the testing of the fission hypothesis. Astron J 82:1013–1024. https://doi.org/10.1086/112164
37. Monaghan JJ (1994) Simulating free surface flows with sph. J Comput Phys 110(2):399–406. https://doi.org/10.1006/jcph.1994.1034
38. Aguirre Bermudez DM, Abraham A, Joshi S, Schwitzke C, Bauer H-J (2024) Numerical Analysis of the Effect of Geometric Variations on the Mass Flow Distribution for an Under-Race Lubrication System. Turbo Expo, Volume 1: Aircraft Engine, pp 001–01011. https://doi.org/10.1115/GT2024-122481
39. Ihmsen M, Cornelis J, Solenthaler B, Horvath C, Teschner M (2014) Implicit incompressible sph. IEEE Trans Vis Comput Graph 20(3):426–435. https://doi.org/10.1109/TVCG.2013.105
40. Akinci N, Akinci G, Teschner M (2013) Versatile surface tension and adhesion for sph fluids. ACM Trans Graph 32(6). https://doi.org/10.1145/2508363.2508395
41. Wilhelmy L (1863) Ueber die abhängigkeit der capillaritäts-constanten des alkohols von substanz und gestalt des benetzten festen körpers. Ann Phys 195(6):177–217. https://doi.org/10.1002/andp.18631950602
42. Hu XY, Adams NA (2006) A multi-phase sph method for macroscopic and mesoscopic flows. J Comput Phys 213(2):844–861. https://doi.org/10.1016/j.jcp.2005.09.001
43. Zhu D, Hu Y-Z (1999) The study of transition from elastohydrodynamic to mixed and boundary lubrication. The advancing frontier of engineering tribology, Proceedings of the 1999 STLE/ASME HS Cheng Tribology Surveillance, 150–156

44. Hansen E, Kacan A, Frohnapfel B, Codrignani A (2022) An ehl extension of the unsteady fbns algorithm. Tribol Lett 70(3):80. https://doi.org/10.1007/s11249-022-01615-1
45. Stephan S, Lautenschläger MP, Alhafez IA, Horsch MT, Urbassek HM, Hasse H (2018) Molecular dynamics simulation study of mechanical effects of lubrication on a nanoscale contact process. Tribol Lett 66:1–13. https://doi.org/10.1007/s11249-018-1076-0
46. Stephan S, Dyga M, Urbassek HM, Hasse H (2019) The influence of lubrication and the solid-fluid interaction on thermodynamic properties in a nanoscopic scratching process. Langmuir 35(51):16948–16960. https://doi.org/10.1021/acs.langmuir.9b01033
47. Thompson AP, Aktulga HM, Berger R, Bolintineanu DS, Brown WM, Crozier PS, In't Veld PJ, Kohlmeyer A, Moore SG, Nguyen TD et al (2022) Lammps-a flexible simulation tool for particle-based materials modeling at the atomic, meso, and continuum scales. Comput Phys Commun 271:108171. https://doi.org/10.1016/j.cpc.2021.108171
48. Surblys D, Matsubara H, Kikugawa G, Ohara T (2019) Application of atomic stress to compute heat flux via molecular dynamics for systems with many-body interactions. Phys Rev E 99(5):051301. https://doi.org/10.1103/PhysRevE.99.051301
49. Etesami SA, Asadi E (2018) Molecular dynamics for near melting temperatures simulations of metals using modified embedded-atom method. J Phys Chem Solids 112:61–72. https://doi.org/10.1016/j.jpcs.2017.09.001
50. Potoff JJ, Bernard-Brunel DA (2009) Mie potentials for phase equilibria calculations: application to alkanes and perfluoroalkanes. J Phys Chem B 113(44):14725–14731. https://doi.org/10.1021/jp9072137
51. Weeks JD, Chandler D, Andersen HC (1971) Role of repulsive forces in determining the equilibrium structure of simple liquids. J Chem Phys 54(12):5237–5247. https://doi.org/10.1016/j.jpcs.2017.09.001
52. Kanhaiya K, Kim S, Im W, Heinz H (2021) Accurate simulation of surfaces and interfaces of ten fcc metals and steel using lennard–jones potentials. npj Comput Mater 7(1):17. https://doi.org/10.1038/s41524-020-00478-1
53. Heinz H, Vaia R, Farmer B, Naik R (2008) Accurate simulation of surfaces and interfaces of face-centered cubic metals using 12–6 and 9–6 lennard-jones potentials. J Phys Chem C 112(44):17281–17290. https://doi.org/10.1021/jp801931d
54. Carman F, Ewen JP, Bresme F, Wu B, Dini D (2024) Molecular simulations of thermal transport across iron oxide-hydrocarbon interfaces. ACS Appl Mater Interfaces 16(43):59452–59467. https://doi.org/10.1021/acsami.4c09434
55. Leroy F, M"uller-Plathe F (2015) Dry-surface simulation method for the determination of the work of adhesion of solid-liquid interfaces. Langmuir 31(30):8335–8345. https://doi.org/10.1021/acs.langmuir.5b01394
56. Avila KE, Vardanyan VH, Alhafez IA, Zimmermann M, Kirsch B, Urbassek HM (2020) Applicability of cutting theory to nanocutting of metallic glasses: atomistic simulation. J Non-Crystalline Solids 550:120363. https://doi.org/10.1016/j.jnoncrysol.2020.120363
57. Beckmann N, Romero P, Linsler D, Dienwiebel M, Stolz U, Moseler M, Gumbsch P (2014) Origins of folding instabilities on polycrystalline metal surfaces. Phys Rev Appl 2(6):064004. https://doi.org/10.1103/PhysRevApplied.2.064004
58. Ta D, Tieu AK, Zhu H, Kosasih B (2015) Thin film lubrication of hexadecane confined by iron and iron oxide surfaces: A crucial role of surface structure. J Chem Phys 143(16). https://doi.org/10.1063/1.4933203
59. Uhlmann E, Barth E, Bock-Marbach B, Kuhnert J (2024) Numerical chip formation analysis during high-pressure cooling in metal machining. CIRP J Manuf Sci Technol 53:103–117. https://doi.org/10.1016/j.cirpj.2024.07.003
60. Denkena B, Poll G, Bergmann B, Pape F, Nassef B, Schenzel J (2025) Influence of cooling lubricants on mechanical load at the cutting wedge using high-speed microcinematography and an open-contra rotation tribometer. CIRP J Manuf Sci Technol 58:40–46. https://doi.org/10.1016/j.cirpj.2025.01.010
61. Choo J, Olver A, Spikes H (2003) Influence of surface roughness features on mixed-film lubrication. Lubr Sci 15(3):219–232. https://doi.org/10.1177/1350650113513572
62. Patel R, Khan ZA, Saeed A, Bakolas V (2022) A review of mixed lubrication modelling and simulation. Tribol Ind 44(1):150–168. https://doi.org/10.1177/1350650113513572
63. Jadhao V, Robbins MO (2017) Probing large viscosities in glass-formers with nonequilibrium simulations. Proceed Natl Acad Sci 114(30):7952–7957. https://doi.org/10.1073/pnas.1705978114
64. Schmitt S, Fleckenstein F, Hasse H, Stephan S (2023) Comparison of force fields for the prediction of thermophysical properties of long linear and branched alkanes. J Phys Chem B 127(8):1789–1802. https://doi.org/10.1021/acs.jpcb.2c07997
65. Evans DJ, Morriss G (1984) Nonlinear-response theory for steady planar couette flow. Phys Rev A 30(3):1528. https://doi.org/10.1103/PhysRevA.30.1528
66. Kalin M, Polajnar M (2014) The wetting of steel, dlc coatings, ceramics and polymers with oils and water: the importance and correlations of surface energy, surface tension, contact angle and spreading. Appl Surface Sci 293:97–108. https://doi.org/10.1016/j.apsusc.2013.12.109
67. Cho H, Chung J, Lee S (2023) Robustly adherable hierarchical nanostructures via self-bonding and self-texturing of aluminum nitride for applications in highly efficient oil/water separation. ACS Omega 8(45):42732–42740. https://doi.org/10.1021/acsomega.3c05524
68. Souza PS, Santos AJ, Cotrim MA, Abrão AM, Câmara MA (2020) Analysis of the surface energy interactions in the tribological behavior of alcrn and tialn coatings. Tribol Int 146:106206. https://doi.org/10.1016/j.triboint.2020.106206
69. Lugscheider E, Bobzin K, Möller M (1999) The effect of pvd layer constitution on surface free energy. Thin Solid Films 355:367–373. https://doi.org/10.1016/S0040-6090(99)00543-X
70. Wróblewski P, Kachel S (2023) The concept of the contact angle in the process of oil film formation in internal combustion piston engines. Sci Rep 13(1):20715. https://doi.org/10.1038/s41598-023-48949-x